

7-9-2009

# Effect of moderate magnetic annealing on the microstructure and mechanical behavior of a structural epoxy

Mehran Tehrani

Follow this and additional works at: [https://digitalrepository.unm.edu/me\\_etds](https://digitalrepository.unm.edu/me_etds)

---

## Recommended Citation

Tehrani, Mehran. "Effect of moderate magnetic annealing on the microstructure and mechanical behavior of a structural epoxy." (2009). [https://digitalrepository.unm.edu/me\\_etds/36](https://digitalrepository.unm.edu/me_etds/36)

This Thesis is brought to you for free and open access by the Engineering ETDs at UNM Digital Repository. It has been accepted for inclusion in Mechanical Engineering ETDs by an authorized administrator of UNM Digital Repository. For more information, please contact [disc@unm.edu](mailto:disc@unm.edu).

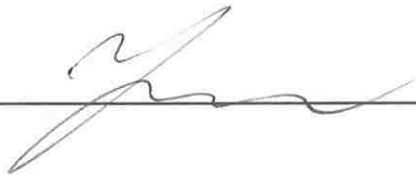
Mehran Tehrani  
*Candidate*

Mechanical Engineering  
*Department*

This thesis is approved, and it is acceptable in quality  
and form for publication on microfilm:

*Approved by the Thesis Committee:*

  
\_\_\_\_\_ Dr. Marwan Al-Haik, Chairperson

  
\_\_\_\_\_ Dr. Yu-Lin Shen

*Zayd Chad Leseman April 14, 2009*  
\_\_\_\_\_ Dr. Zayd Leseman

*Claudia Luhrs 04/14/09*  
\_\_\_\_\_ Dr. Claudia Luhrs

\_\_\_\_\_  
\_\_\_\_\_  
\_\_\_\_\_

Accepted:

\_\_\_\_\_ *Dean, Graduate School*

\_\_\_\_\_ *Date*

**Effect of Moderate Magnetic Annealing on the  
Microstructure and Mechanical Behavior of a Structural  
Epoxy**

**BY**

**MEHRAN TEHRANI**

**SHARIF UNIVERSITY OF TECHNOLOGY  
JUNE 2007**

THESIS

Submitted in Partial Fulfillment of the  
Requirements for the Degree of

Master of Science in Mechanical  
Engineering

The University of New Mexico  
Albuquerque, New Mexico  
**May 2009**

## **DEDICATIONS**

This thesis would be incomplete without a mention of the support given to me by my parents, to whom this thesis is dedicated.

## **ACKNOWLEDGEMENTS**

First, I would like to thank my advisor Prof. Al-Haik for his consistent support and patient guidance throughout this project. I benefited a lot from Prof. Al-Haik's keen insight of complicated problems and his useful suggestions. I would like to mention that Prof. Al-Haik has helped me not only as an advisor, but also as a really good friend in all the vicissitudes I have had being a new international student. I would also like to thank Dr. Dongsheng Li at Georgia Institute of Technology, School of Materials Science, who has helped me a great deal with the texture part of the experiments.

**Effect of Moderate Magnetic Annealing on the  
Microstructure and Mechanical Behavior of a Structural  
Epoxy**

**BY**

**MEHRAN TEHRANI**

ABSTRACT OF THESIS

Submitted in Partial Fulfillment of the  
Requirements for the Degree of

Master of Science in mechanical  
Engineering

The University of New Mexico  
Albuquerque, New Mexico

**May, 2009**

# **Effect of Moderate Magnetic Annealing on the Microstructure and Mechanical Behavior of a Structural Epoxy**

**By:**

**Mehran Tehrani**

**B.S., Mechanical Engineering, Sharif University of technology, 2007**

**M.S., Mechanical Engineering, University of New Mexico, 2009**

## **ABSTRACT**

The effect of a moderate permanent magnetic field (i.e., 0.50 Tesla) on a structural epoxy has been investigated. The magnetic field induced-changes on the microstructure of the epoxy system were probed through wide-angle x-ray diffraction (WAXD) and texture analysis. Pole figures were generated for all the samples along the directions parallel and perpendicular to the applied magnetic field. This allowed, quantitatively, comparing the textures and fully understanding the mechanisms that result in a preferred orientation generation. The texture analysis revealed that under such moderate magnetic field and due to the diamagnetism of the epoxy system, the chains and the cross linking reorient biaxially in a plane that shares the magnetic field direction. The evolution of mechanical properties (modulus, hardness and toughness) under different thermo-mechanical environment was investigated using the instrumented nanoindentation. Improvements in both Young's modulus and hardness by up to 6.6% were observed in the transverse direction of the magnetic field. However, evident by the measured elastic and plastic work under nanoindentation, it was observed that the magnetically annealed sample encountered slight embrittlement. Furthermore, the current study reports enhancement on the mechanical properties of the epoxy when the nanoindentation tests are carried out under elevated temperatures (50-70 °C) below the glass transition temperature of the epoxy. The time-dependent behavior of the epoxy was investigated under different thermal environments on light of the magnetic annealing- induced texture. The storage and loss moduli together with tan-delta as measures of the viscoelastic behavior of the polymer were measured using the continuous contact compliance module of the nanoindenter. The results of the current study showed that even under relatively low magnetic fields the mechanical properties, creep resistance and viscoelastic properties of the structural epoxy have been improved; tan-delta was measured to be 9.8% less for magnetically annealed compared to the neat epoxy sample.

## Table of Contents

<b>LIST OF FIGURES</b> .....	vii
<b>LIST OF TABLES</b> .....	ix
 <b>CHAPTER 1: BACKGROUND AND THESIS OUTLINE</b>	
1.1 Introduction.....	1
1.2 Thesis Motivation.....	4
1.3 Thesis Outline.....	6
 <b>CHAPTER 2: ORIENTATION CHARACTERIZATION OF MAGNETICALLY ANNEALED EPOXY</b>	
2.1 Orientation Representation for Amorphous Polymers.....	7
2.2 Texture Analysis of Polymers.....	9
2.3 Epoxy System.....	15
2.4 Magnetic processing Experiment.....	18
2.5 WAXD Measurements.....	20
2.6 Texture results.....	22
 <b>CHAPTER 3: NANOINDENTATION TESTS AT AMBIENT AND ELEVATED TEMPERATURES</b>	
3.1 The Nano Test System.....	33
3.2 Nanoindentation Data Analysis.....	36
3.3 Nanoindentation of Viscoelastic Materials .....	43
3.4 Nanoindentation Results.....	44
3.5 Uncertainties in Nanoindentation Measurements for Viscoelastic Materials.....	47
3.6 Hot Stage Nanoindentation.....	50
 <b>CHAPTER 4: EFFECT OF MAGNETIC ANNEALING ON TIME –DEPENDENT BEHAVIOR</b>	
4.1 Nanocreep Test.....	56
4.2 Continuous Compliance Calculations .....	59
 <b>CHAPTER 5: CONCLUSIONS AND FUTURE WORK</b>	
5.1 Conclusions.....	68
5.2 Future work.....	71
<b>REFERENCES</b> .....	73



## List of Figures

<b>Figure 2-1:</b> Schematic diagrams of phase transition and structure development during an amorphous polymer reorientation. After Kawakami et al. [1].....	8
<b>Figure 2-2:</b> Stereographic projection illustrating the projection of a 3D sphere onto a 2D plane [2].....	11
<b>Figure 2-3</b> Definition of the $\alpha$ and $\beta$ angles in the sample reference frame. At a sample rotation of $0^\circ$ : The $y_1$ direction is the incident X-ray beam axis; the $y_2$ direction is perpendicular to both the incident beam and the sample rotation axis; the $y_3$ axis is the sample rotation axis.....	12
<b>Figure 2-4</b> Relationships between the Bragg reflection angle ( $\theta$ ), azimuthal angle ( $\phi$ ), and goniometer rotation angle ( $\eta$ ) and the plate normal, S.....	13
<b>Figure 2-5:</b> Schematic of the magnetic processing of the samples. The figure shows the axial and lateral directions of the sample with respect to the direction of the maximum magnetic field.....	18
<b>Figure 2-6</b> The $2\theta$ scan of a magnetically annealed sample. The scan was performed at a point close to the edge of the sample where the magnetic field is maximized.....	21
<b>Figure 2-7</b> The $2\theta$ scan of a neat epoxy sample at the lower edge of the container. The scan was performed at a point close to the edge of the sample where the magnetic field is maximized.....	21
<b>Figure 2-8:</b> Schematic illustration of four different locations at which individual pole figures analysis was carried out.....	23
<b>Figure 2-9:</b> WAXD azimuthal-radial scan at location M1 for magnetically annealed epoxy sample.....	24
<b>Figure 2-10:</b> WAXD azimuthal-radial scan at location M1 for neat epoxy sample.....	24
<b>Figure 2-11:</b> WAXD azimuthal-radial scan at location L1 for magnetically annealed epoxy sample.....	25
<b>Figure 2-12:</b> WAXD Azimuthal-radial scan at location L1 for neat epoxy sample.....	25
<b>Figure 2-13:</b> Pole figures generated at location M1 for (a) neat epoxy sample and (b) magnetically annealed epoxy.....	27
<b>Figure 2-14:</b> Pole figures generated at location M2 for (a) neat epoxy sample and (b) magnetically annealed epoxy.....	28
<b>Figure 2-15:</b> Pole figures generated at location L1 for (a) neat epoxy sample and (b) magnetically annealed epoxy.....	29
<b>Figure 2-16:</b> Pole figures generated at location L2 for (a) neat epoxy sample and (b) Magnetically annealed epoxy.....	30
<b>Figure 2-17:</b> The two-dimensional stretching effect a magnetic field exerts on the main chains and crosslinks of an epoxy.....	32
<b>Figure 3-1:</b> Schematic of the NanoTest with two different views of the Berkovich indenter (Micro Materials Ltd.).....	34
<b>Figure 3-2:</b> (a) Typical loading vs. indenter displacement curve (b) cross-section of a Berkovich indenter trace in the sample.....	37
<b>Figure 3-3:</b> DAF for the Berkovich tip used in this study.....	39

<b>Figure 3-4:</b> Schematic of Loading/Unloading vs. time for an indentation.....	40
<b>Figure 3-5:</b> A representative indentation curve on the polymer of the current study with creep and thermal drift data collected.....	41
<b>Figure 3-6:</b> Creep of the sample at maximum load.....	41
<b>Figure 3-7:</b> Thermal drift data collected at 90% of unloading.....	42
<b>Figure 3-8:</b> Plastic and Elastic work for an indentation.....	43
<b>Figure 3-9:</b> Nanoindentation load–displacement hysteresis of a sample that was magnetically processed. The maximum loads applied were 1, 3 and 5 mN, respectively, at a loading rate of 0.05 mN/sec and unloading rate of 0.1 mN/sec.....	44
<b>Figure 3-10:</b> Nanoindentation load–displacement hysteresis of a sample that was not magnetically processed. The maximum loads applied were 1, 3 and 5 mN, respectively, at a loading rate of 0.05mN/sec and unloading rate of 0.1 mN/sec.....	45
<b>Figure 3-11:</b> 3-D AFM scan of an indentation.....	48
<b>Figure 3-12:</b> 2-D AFM scan of an indentation with the cross section showing the pile up.....	49
<b>Figure 3-13:</b> Schematic of the NanoTest with the hot stage (HS) installed [3].....	50
<b>Figure 3-14:</b> The set up for the Hot Stage.....	51
<b>Figure 3-15:</b> Reduced elastic modulus for magnetically annealed, M, and neat sample, N, at elevated temperatures of 50°C and 70°C. The sample cures as the test is progressing. The horizontal axis corresponds to time or test number. Duration between each two tests is 15 minutes.....	53
<b>Figure 3-16:</b> Hardness for magnetically annealed, M, and neat sample, N, at elevated temperatures of 50°C and 70°C. The sample cures as the test is progressing. The horizontal axis corresponds to time or test number. Duration between each two tests is 15 minutes.....	54
<b>Figure 3-17:</b> Plastic and Elastic work magnetically annealed, M, and neat sample, N, at elevated temperatures of 50°C and 70°C. The sample cures as the test is progressing. The horizontal axis corresponds to time or test number. Duration between each two tests is 15 minutes.....	54
<b>Figure 4-1:</b> Depth vs. time nanoindentation creep curve for the polymer sample, maximum load 5 mN and loading rate of 0.5 mN/s were applied.....	56
<b>Figure 4-2:</b> Nanocreep tests of epoxy samples at ambient temperature. A maximum load of 1 mN was held constant for 2700 s during the test. M and N correspond to magnetically annealed and neat sample, respectively.....	58
<b>Figure 4-3:</b> Nanocreep tests of epoxy samples in lateral direction at elevated temperatures of 50 and 70 °C. A maximum load of 1 mN was held constant for 2700 s during the test. M and N correspond to magnetically annealed and neat sample respectively.....	58
<b>Figure 4-4:</b> Spring dashpot model for the continuous contact compliance measurement.....	61
<b>Figure 4-5:</b> Spring dashpot model of the test setup with the sample in place [88].....	62

**Figure 4-6:** Spring dashpot model with the calibration spring in place [88].....63

**Figure 4-7:** Cyclic load-hold-partial unload indentations on epoxy for measuring phase during hold period.....65

**Figure 4-8:** Cross section of a nanoindentation showing pile up.....66

**Figure 4-9:** A representative of the model fit to the experimental phase shift versus depth curve of the polymer sample.....67

## List of Tables

<b>Table 2-1</b> Physical and mechanical properties of the epoxy system.....	17
<b>Table 3-1</b> Mechanical properties for magnetically annealed and neat samples in both lateral and axial directions.....	47
<b>Table 4-1</b> Viscoelastic properties measured in the ND direction on the lateral side of the Samples.....	67

# CHAPTER 1: BACKGROUND AND THESIS OUTLINE

## 1.1 Introduction

Thermosets prepared via curing liquid crystalline monomers possess novel mechanical and physical properties. Due to their excellent mechanical properties, compared to thermoplastics, epoxies are used extensively as matrices in the fabrication of fiber reinforced plastics (FRPs) both at the micro scale, using micro scale carbon fibers [4], and at the nanoscale using carbon nanotubes [5]. Furthermore, due to their optical anisotropy, liquid crystals have potential in a wide range of applications including optical filters, displays, and data storage [6]. They have also been widely used in forms of bulk neat resin, coatings, adhesives, and thin films and recently in biomedical applications and MEMS/NEMS industry.

The mechanical and physical properties of molecular materials such as polymers are strongly influenced not only by the molecular structure of the epoxies [7] but also by their molecular deformation and orientation behavior of their chains [8]. Improving these properties can be achieved by manipulating the spatial arrangement of the molecules at the nanoscale via self-organization of the chains [9]. At the macro scale introducing texture can be fulfilled by super molecular chemistry or by introducing alignment [10].

In some studies chains alignment was induced by flow (shear) fields methods, such as extrusion [11] and injection molding [12]. Most of these techniques produce a morphology that comprises of an oriented shell of the polymer with a relatively unoriented inner core. This uneven shell-core orientation is attributed to rheological and interfacial properties of the constituent components (such as shear viscosity, fluid elasticity and interfacial tension); blend composition; and processing variables (such as curing temperature and shear rate) [13].

Since the use of flow fields poses several limitations on the types of epoxies that can be processed, several investigations explored the use of other fields such as electrical and magnetic fields or a combination of both [14-16].

Shiota et al. (1997) investigated the curing of liquid crystalline (LC) epoxies under applied AC electric fields. The investigators observed that the extent of polymerization has strongly influenced the molecular response to the AC electric fields, the final networks could be aligned only perpendicular to the electric field. The oriented network possessed high orientation as well as high translational order. Controlling the orientation of organic molecules with electric fields plays an important role in commercially important devices, such as liquid crystalline displays (LCDs). The ability of electric fields to induce the controlled alignment of lyotropic liquid crystalline polymer thin films on micro fabricated substrates was demonstrated by Martin [17]. The polymers were oriented by the electric field while in solution and solidified into a stable, oriented structure by solvent evaporation.

Magnetic field induced-alignment of polymeric materials has been the focus of numerous investigations [10, 14, 16, 18-27]. Unlike the flow fields, magnetic fields effective strength does not decrease in the center of the sample, and thus the formation of the core-shell morphology is unlikely [20].

Polymeric materials can reorient inside a magnetic field through the diamagnetic anisotropy of the constituent chemical units, provided that the magnetic anisotropy and/or the size of the molecules is sufficiently large [10]. The energy that the chemical unit gains through the interaction with an external magnetic field is dependent on the orientation of the unit relative to the magnetic field, and hence the unit tends to align in a direction that would minimize its energy [27]. The idea of magnetic induced alignment is to orient a liquid crystalline monomer in an external field and subsequently freeze the orientation by polymerization and curing, thermally, chemically, or photochemically. Obviously, the macroscopic ordering might be irreversibly fixed by the chemical reaction, resulting in texture generated anisotropy in the physical and mechanical properties [26].

In addition to reorienting the polymer itself, sometimes aligning the polymer chains can be utilized to facilitate the alignment of other materials embedded in the polymer such as carbon nanotubes both single wall [5] and multiwall [28].

There have been shown significant improvements in mechanical, electrical optical and thermal properties of polymeric materials processed under high magnetic fields [29]. But few published works have utilized low magnetic fields (i.e., lower than 1 Tesla). Low magnetic fields have been used to affect the polymerization of methyl acrylate by changing the molecular weight of the cured polymers [30]. When the viscosity is low the molecules thermal agitation energy to overcome is less, so the diamagnetic forces are more likely to produce a texture in the polymer.

The major reason for using the high magnetic fields ( $> 1$  Tesla) is that using the laws of continuum mechanics and thermodynamics it was shown that polymer alignment does not favor low magnetic fields [23]. From the continuum point of view owing to the diamagnetic anisotropy of chemical bonds, organic molecules have a potential ability to align under a magnetic field [31]. Organic crystals [32, 33] and polymeric fibers, [34-38] which exhibit anisotropic diamagnetic susceptibility, can undergo magnetic alignment in suspension, if their size is large enough to exceed the thermal agitation energy. The minimum size required for the magnetic alignment ranges from micrometers to tens of nanometers depending on the values of the diamagnetic anisotropy (typically  $-10 \times 10^{-5} - 10^{-7}$  emu/mol) of the material and the field strength used (5 – 10 Tesla)[29].

Based on earlier work by Garmestani et al. [5] the alignment of single wall carbon nanotubes (SWCNTs) in high viscosity epoxy utilizing high magnetic field of 15-25 Tesla was documented. That alignment occurred at magnetic field, though 15-25 Tesla high, is still much lower than the calculated theoretical field strength values based on continuum approach. Later, Al-Haik and Hussaini utilized molecular dynamics simulation to explain the alignment of polymers under magnetic field [39]. Later they used the same approach to explain how the alignment of polymers could mediate the alignment of SWCNTs [40].

Besides the valid computational tools at nanoscale such as molecular dynamics, there is a pressing need for experimental techniques to examine the polymer alignment and to investigate the degree of improvements on the polymer mechanical properties upon reorientation.

Diamagnetism aligns the polymer molecules either parallel or perpendicular to the field [23, 24, 41]. This can be characterized in the light of wide-angle x-ray diffraction (WAXD) and scanning electron microscopy (SEM) imaging of the fracture surface. SEM will be a valid tool only if the field is large enough to produce a strong and visible texture (fibril). Alternatively, the induced alignment can be investigated indirectly by mechanically testing the samples along different directions with respect to the magnetic field direction [18].

## **1.2 Thesis motivation**

Despite the numerous literatures citing success in utilizing high magnetic fields to align polymers, fewer citations could be found for utilizing low magnetic fields based on permanent magnets.

Moreover, in the few citations found, there were some controversies and contradictions cited by rival groups! For example, scientist from the former Soviet Union have carried out major researches back in the 70's regarding modifying high temperature curing resin systems under low magnetic fields and they have reported improvements in mechanical, optical and thermal properties in different cases [42-44]. Gerzeski [45] showed significant modifications of some of the mechanical properties under fields as low as 0.38 Tesla but showed no improvement in Young's modulus for most of the epoxies at the macro scale. It is worth to mention that both groups conducted their mechanical testing at the macroscale; using a tensile machine and while the Soviets reported some improvements on the elastic modulus and hardness, the US-based group at the AFRL reported no such improvements.

It is rather strange that neither group tried to investigate the microstructure of the epoxy upon magnetic processing! Thus, one theory is: there might have been some improvements but the tool to measure the change in the microstructure and the changes in



mechanical properties were inappropriate in the previous literature. Investigating the microstructure was carried out for numerous high magnetic field processing investigations such as Kimura et al. [23] and Al-Haik et al. [18] where they investigated the magnetically induced changes on microstructures using WAXD, pole figures and ESEM analysis.

Thus in this thesis WAXD and texture analysis of both before and after magnetic annealing of epoxy will be investigated at different locations on the samples along different orientations with respect to the magnetic field direction. The improvement in mechanical properties will be measured using very accurate technique that can detect very small changes; nanoindentation rather than macroscale tensile testing. Furthermore, the effect of the annealing temperature will be also investigated.

Furthermore, it is well known that regardless of the improvement in static mechanical properties, polymers exhibit significant creep deformation under even low loads or even at room temperature. Therefore, improving creep properties of polymeric materials is of high interest as well. Viscoelastic characterization methods such as creep, relaxation and dynamic mechanical analysis (DMA) tests needs to be utilized to measure the degree of improvement on viscoelastic behavior [41, 46, 47]. Currently, there are very few investigations regarding how magnetic processing will affect the long term time-dependant performance of these polymers [48].

Hence, in this thesis the creep of the samples before and after magnetic annealing will be investigated under constant load and three different temperatures ranging from room temperature to a temperature that is close to the glass transition of the polymer. For longer-term creep, the thesis will present the effect of magnetic processing through utilizing continuous contact compliance (CCC); i.e. through measuring the changes in loss and storage moduli.

### **1.3 Thesis Outline**

The introductory chapter of this MS thesis summarizes the background on the state of the art in the field of magnetic processing of polymeric materials together with some current challenges and several aspects that have been overlooked under previous investigations. In Chapter two, a brief description about the use of WAXD and pole figure analysis to describe the orientation of the oriented amorphous epoxy is presented. The description of the epoxy system, the samples processing using 0.5 Tesla magnetic field, and complete microstructure analysis using WAXD 2- $\theta$  scan and azimuthal scans are presented toward the construction of pole figures using the software PopLA. In Chapter 3, mechanical analysis of the effect of magnetic processing on the samples is carried out using nanoindentation. Nanoindentation was carried out along the magnetic field and the lateral direction at different maximum loads. Furthermore, the affect of curing the samples post-magnetic processing under elevated temperatures is also investigated. Chapter 4 highlights the effect of magnetic processing on the creep properties of the polymeric system utilized through nanocreep tests coupled with continuous contact compliance analysis; loss and storage moduli analysis on light of the magnetic processing. The thesis concludes in Chapter 5 by presenting major findings and some future proposed work.

## **CHAPTER 2: ORIENTATION CHARACTERIZATION OF MAGNETICALLY ANNEALED EPOXY**

### **2.1 Orientation Representation for Amorphous Polymers**

Epoxies are generally treated as a two-phase system comprising crystalline lamellae and noncrystalline segments outside the lamella. The noncrystalline phase is usually referred to as amorphous phase, although it is commonly understood that the amorphous chain segments outside the lamellae can have some local order.

An amorphous polymer does not exhibit a crystalline X-ray diffraction pattern. If the structure of crystalline polymers is taken to be regular or ordered, then by difference, the structure of amorphous polymers contains greater amounts of disorder. The older literature often referred to the amorphous state as a liquid state. Today, amorphous polymers in the glassy state are typically called amorphous solids.

Schematically, the structure of bulk amorphous polymers has been linked to a pot of spaghetti, where the spaghetti strands weave randomly in and out among each other. The spaghetti model provides an entry into the question of partial order in amorphous polymers.

Assuming that the initial sample consists of only isotropic amorphous chains, Figure 2-1(a), upon applying an external field, some amorphous chains will become oriented, Figure 2-1 (b), and can transform into fibrillar structure. Based on previous work of Al-Haik et al.[49], the length of the fibril can extend to several micrometers if the external magnetic field strength is very high; above 15 Tesla.

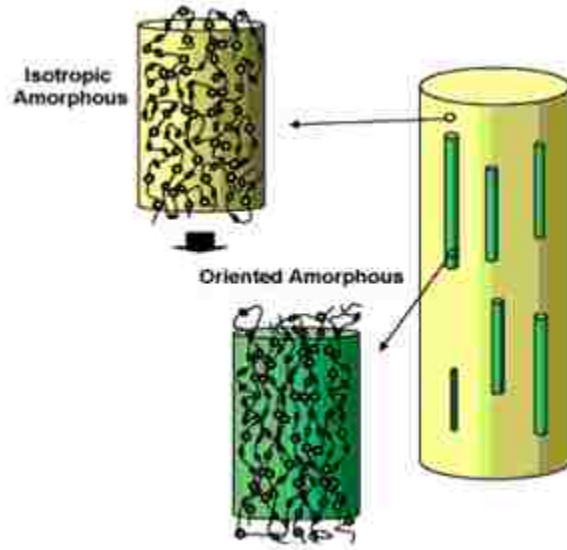


**Figure 2-1:** Schematic diagrams of phase transition and structure development during an amorphous polymer reorientation. After Kawakami et al. [1].

The extent of the short-to-medium range order within the amorphous phase, the density, orientation and the conformation of the amorphous chain segments profoundly influence the mechanical performance of the polymer. In particular, modulus, tenacity and diffusion are influenced by the amorphous orientation [50].

There are several techniques to explore the orientation in amorphous phase orientation. These include optical birefringence and sonic modulus [50]. The optical birefringence depends on the difference between the refractive index of the oriented domains along and perpendicular to a fiber axis. The sonic modulus depends on the variation in the acoustic speed with orientation of the amorphous region. Both these techniques require the knowledge of the crystallinity of the polymer and both have inherent limitations. For example the amorphous orientation obtained via the birefringence data- and crystallinity by default- could be ambiguous if the correct values of the intrinsic birefringence of the crystalline and amorphous domains are not well known. Likewise, prior knowledge of the modulus of the crystalline and amorphous domains is essential before using the sonic modulus method.

Because of these shortcomings of the above mentioned techniques, it is widely accepted to use the wide angle x-ray diffraction (WAXD) method to evaluate the amorphous orientation [1, 33, 50-53]. Under various conditions, crystalline substances diffract X-rays and electrons to give spots or rings. Amorphous materials, also diffract X-rays and electrons, but the diffraction is much more diffuse, sometimes called halos [54].

There are a number of differences between x-ray diffraction in polymers and metallurgical or ceramic diffraction [51].

- Polymers are not highly absorbing to x-rays. The dominant experiment is a transmission experiment where the x-ray beam passes through the sample. This greatly simplifies analysis of diffraction spectra for polymers but requires somewhat specialized diffractometer from those commonly used for metallurgy (usually a reflection experiment).
- Polymers are never 100% crystalline. XRD is a primary technique to determine the degree of crystallinity in polymers.
- Synthetic polymers almost never occur as single crystals. The diffraction pattern from polymers is almost always either a "powder" pattern (polycrystalline) or a fiber pattern (oriented polycrystalline).
- Polymers, due to their long chain structure, are highly susceptible to orientation. XRD is a primary tool for the determination of crystalline orientation.
- For semi-crystalline polymer crystals display a relatively large number of defects in some cases. This leads to diffraction peak broadening.
- Polymer crystallites are very small with a large surface to volume ratio which enhances the contribution of interfacial disorganization on the diffraction pattern.

## **2.2 Texture Analysis of Polymers**

There are numerous techniques to quantify the preferred orientation, or "texture" of materials, to name some:

- X-ray diffraction; pole figures; measures *average* texture at a surface (microns penetration); projection (2 angles).
- Neutron diffraction; type of data depends on neutron source; measures *average* texture in bulk (centimeters penetration in most materials); projection (2 angles).
- Electron [back scatter] diffraction; easiest [to automate] in scanning electron microscopy (SEM); *local* surface texture (nanometers penetration in most materials); complete orientation (3 angles).
- Polarized optical microscopy: optical activity (plane of polarization); limited information (one angle).

X-ray pole figures are the most common source of texture information; cheapest, easiest to perform. They have the advantage of providing an average texture over a reasonably large surface area ( $\sim 1\text{mm}^2$ ), compared to EBSD [2].

For crystalline materials the pole figure is a presentation of the three-dimensional orientation of a crystalline plane. On a pole figure map, one may observe both the location and intensity of the orientation of a crystalline plane with respect to the x, y, and z reference directions. The intensity in the poles represents the variation in diffracted intensity of specific crystal direction with respect to sample reference frame. More concretely, it is the frequency of occurrence of a given crystal plane normal per unit spherical area.

Stereographic pole figures are one method of projecting a three dimensional sphere onto a two dimensional plane. Lines drawn from the southern pole of the sphere end at points on the northern hemisphere. Where these lines intersect the horizontal plane defined by the north-south axis of the sphere is where the orientation defined by each line is projected onto the plane. An illustration is shown in Figure 2-2.

Pole figures show the density of crystallographic poles of certain planes as a function of orientation, and so provide a good method of representing orientation. A pole is the point of intersection of the normal to a crystal plane with the surface of a sphere having the crystal at its center. If the crystallite orientation is completely random, the poles will be scattered all over the stereographic projection. If orientation is present, on

the other hand, the poles will tend to be concentrated in certain areas within the projection, while the remaining areas will be completely unpopulated.

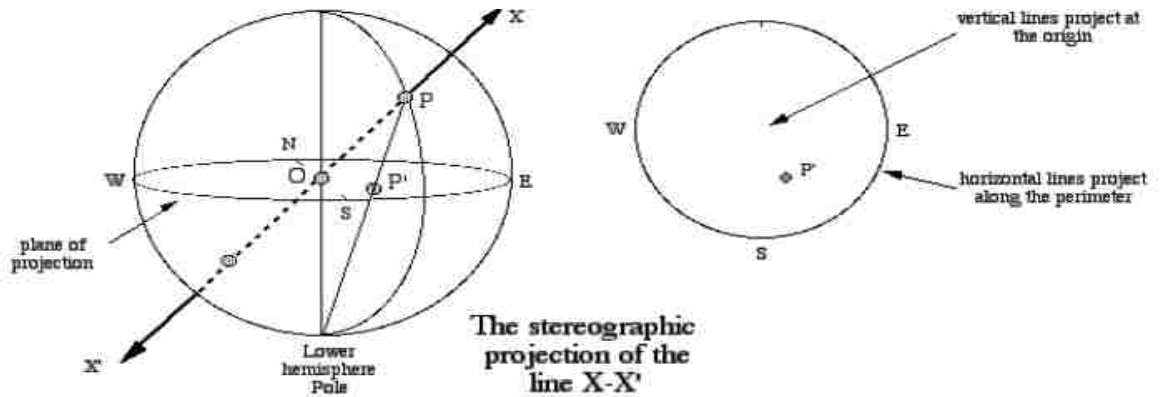


**Figure 2-2:** Stereographic projection illustrating the projection of a 3D sphere onto a 2D plane [2].

Two angles were defined to describe the orientation of the sample, named alpha and beta. Alpha was defined as the angle the plate normal forms with the sample rotation axis, which is perpendicular to the incident beam axis. Beta was the angle in the plane defined by the sample rotation axis (rolling direction, RD) and the transverse direction (TD) in the sample coordinate system from the axis parallel to the incident beam (normal direction, ND) at a sample rotation of  $\eta = 0^\circ$ . A visualization is shown in Figure 2-3.

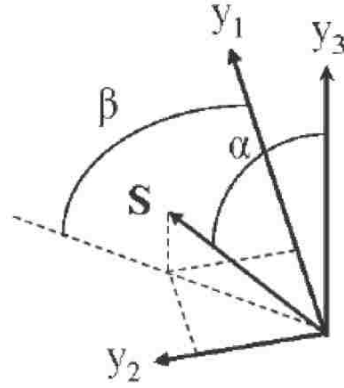


**Figure 2-3** Definition of the  $\alpha$  and  $\beta$  angles in the sample reference frame. At a sample rotation of  $0^\circ$ : The  $y_1$  direction is the incident X-ray beam axis; the  $y_2$  direction is perpendicular to both the incident beam and the sample rotation axis; the  $y_3$  axis is the sample rotation axis.

The plate normal,  $S$ , was calculated based on the angles  $\theta$ ,  $\phi$ . The first step to relating these values was to define the incident beam unit vector and determine the reflected beam unit vector in terms of  $\theta$ ,  $\phi$  and  $\eta$  in the diffractometer coordinate system as shown in Figure 2-4:

$$r_x = \begin{pmatrix} \cos 2\theta \\ \sin 2\theta \cos \phi \\ \sin 2\theta \sin \phi \end{pmatrix}, p_x = \begin{pmatrix} 1 \\ 0 \\ 0 \end{pmatrix} \quad (2-1)$$

The vector representing the plate normal, which is not a unit vector, is found by the difference between the incident beam unit vector,  $\mathbf{p}$ , and the reflected beam unit vector,  $\mathbf{r}$ . Before normalization,  $\mathbf{S}$  is:

$$S = r_x - p_x \quad (2-2)$$

$$S = \begin{pmatrix} -2 \sin^2 \theta \\ 2 \sin \theta \cos \theta \cos \phi \\ 2 \sin \theta \cos \theta \sin \phi \end{pmatrix} \quad (2-3)$$



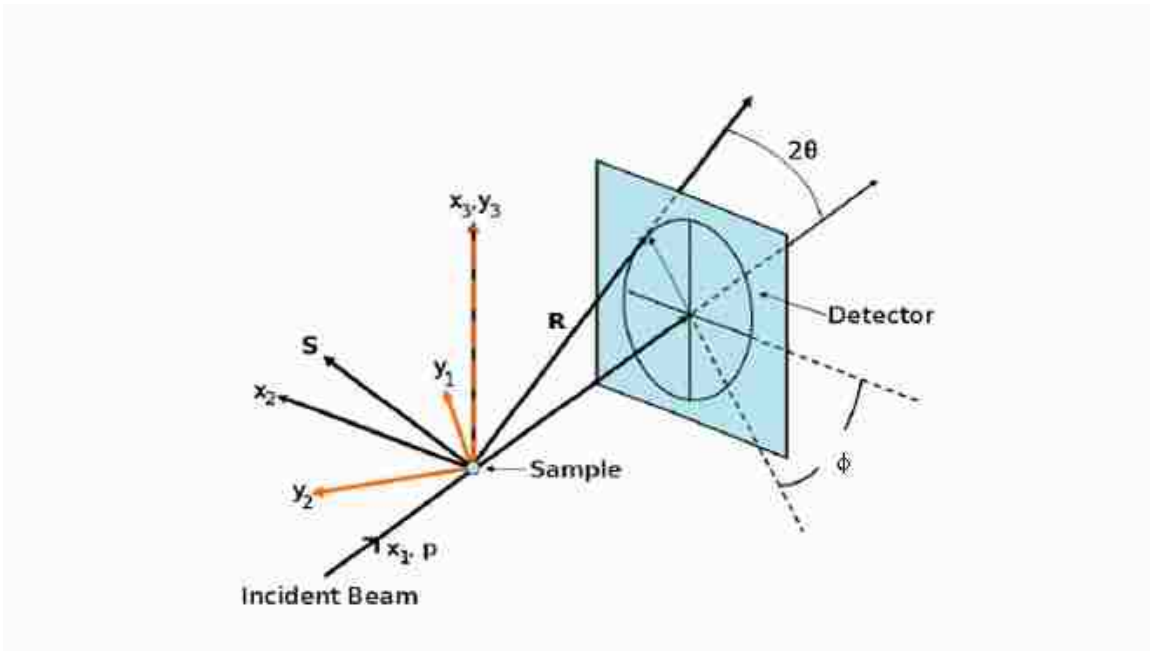


**Figure 2-4** Relationships between the Bragg reflection angle ( $\theta$ ), azimuthal angle ( $\phi$ ), and goniometer rotation angle ( $\eta$ ) and the plate normal,  $S$ .

After normalization,  $S$  becomes the unit vector  $s$

$$s = \begin{pmatrix} -\sin \theta \\ \cos \theta \cos \phi \\ \cos \theta \sin \phi \end{pmatrix} \quad (2-4)$$

The same unit vector  $s$ , was calculated using simple trigonometric relations in terms of the pole figure angles  $\alpha$  and  $\beta$ .

$$s = \begin{pmatrix} \sin \alpha \cos \beta \\ \sin \alpha \sin \beta \\ \cos \alpha \end{pmatrix} \quad (2-5)$$

The two representations of  $s$  were then equated

$$s = \begin{pmatrix} \sin \alpha \cos \beta \\ \sin \alpha \sin \beta \\ \cos \alpha \end{pmatrix} = \begin{pmatrix} -2 \sin^2 \theta \\ 2 \sin \theta \cos \theta \cos \phi \\ 2 \sin \theta \cos \theta \sin \phi \end{pmatrix} \quad (2-6)$$

where  $\alpha$  and  $\beta$  can be represented in terms of  $\theta$ ,  $\phi$  and  $\eta$  as shown in the following equations

$$\begin{aligned} \alpha &= \cos^{-1}(\cos \theta \sin \phi) \\ \beta &= \tan^{-1} \left( \frac{-\sin \eta \sin \theta + \cos \eta \cos \theta \cos \phi}{-\cos \eta \sin \theta - \sin \eta \cos \theta \cos \phi} \right) \end{aligned} \quad (2-7)$$

The total intensity of the diffracted X-rays at any point  $(\alpha, \beta)$  on the  $(hkl)$  pole figure is given by [2]:

$$P_{(hkl)}(\alpha, \beta) = \frac{1}{2\pi} \int_0^{2\pi} f(\eta, \theta, \phi) d\Gamma \quad (2-8)$$

Here  $\Gamma$  denote the path through the orientation distribution corresponding to rotation about the  $(hkl)$  pole. Expansion of the above equation in a series of spherical harmonic functions yields

$$P_{(hkl)}(\alpha, \beta) = \sum_{l=0}^{\infty} \sum_{m=-l}^l Q_{lm} P_l^m(\cos \alpha) e^{im\beta} \quad (2-9)$$

where  $P_l^m(\cos \alpha) e^{im\beta}$  is a spherical harmonic function,  $l$  is the order of the spherical harmonic function and

$$Q_{lm} = \sum_{n=-l}^l W_{lmn} P_l^n(\cos \varphi) e^{-im\eta} \quad (2-10)$$

where  $W_{lmn}$  are the coefficients of the spherical harmonic functions, and  $\varphi$  and  $\eta$  are the polar coordinates of  $(hkl)$  pole in the crystal coordinate systems. By measuring pole

figures of multiple geometrically independent poles we can obtain a set of linear simultaneous equations that can be solved for the  $W_{lmn}$ .

### **Pole Figure Analogy for Noncrystalline Materials:**

For an oriented amorphous material, the relative intensity of the Bragg's peaks varies as the sample is rotated with respect to the incident beam, and it is the graphical display of this intensity variation plotted as a function of the sample tilt which generates the pole figure. A separate pole figure can be obtained for each different Bragg diffraction condition that is satisfied by the sample, and is of sufficient intensity to be monitored as the sample is tilted about the Euler angles. In an amorphous sample the angle  $\theta$  at which complete set of data is collected is not a Bragg angle, but rather as a fixed angle at which one monitors the intensity of the amorphous halo. Thus, the pole figure for amorphous material can be thought of as providing a statistical average of the chains axes with respect to some preferred processing direction (e.g. magnetic field orientation, or mechanical drawing direction).

## **2.3 Epoxy System**

As mentioned in the first chapter, the degree of alignment from the continuum view of point depends on parameters such as activation energy, length and molecular weight of the chains and strength of the field. It also depends on certain chemical groups in the epoxy systems, which diamagnetically align either parallel or perpendicular to the field.

Most of the previous studies on magnetically aligned resin systems have used high viscosity polymers (about 20-120 poise). We believe that if the active diamagnetic chains are present, the lower the viscosities the more probable are the chains to produce a texture. Our resin system has a viscosity of 900-950 centipoises, when it is mixed with the hardener initially.

**Aeropoxy:**

PR2032 is a medium viscosity, unfilled, light amber laminating resin that is designed for structural production applications [47, 55].

This polymer is mostly used in structural applications and composites. It has been magnetically annealed in a study by Al-Haik et al. [49] under magnetic fields of 15-25 Tesla.

When used with the hardener, PH3660, the combination provides excellent wet-out of fiberglass, carbon and aramid fibers. Special additives have been incorporated into this product to promote chemical adhesion to fabrics made with these fibers. Typical applications include aircraft and sail plane skins and structural components, auto bodies, radomes and prototype parts.

Hardener PH3660 is the standard hardener typically used to fabricate high performance composite parts. PH3660 has a one-hour working time. In sufficient mass, both of these hardeners will cure completely at room temperature ( $77^{\circ}F$  or above). For small amounts or layered composites PH3660 will require only moderate heat to become hard. The higher the curing temperature, the higher the resulting service temperature. With a higher temperature cure, a safe service temperature over  $200^{\circ}F$  can be obtained. According to the specifications furnished by the manufacturer (PTM&W Industries, Inc.), the components of the epoxy used here are Aeropoxy PR2032, a material containing diphenylolpropane (bisphenol-A) and a multifunctional acrylate; the hardener component Aeropoxy PH3660 is a modified amine mixture. The epoxy contains also some acrylic monomers. These materials do not contain any metallic compounds of any kind. The absence of metallic compounds in the epoxy resin eliminates the possibility of metallic-induced orientation of the polymer chains and crosslinks, and attributes the response to the magnetic field to the polymer network itself.

These products can be considered low toxicity materials that have minimum hazard potential when used properly and in a clean and responsible manner. PR2032 does not contain any hazardous diluents or extenders. Hardener PH3660 does not contain methylene dianiline (MDA), or other potentially harmful aniline derivatives. Neither the resin nor the hardeners will crystallize in normal shipping and storage conditions,

including refrigerated storage. Both components have excellent moisture resistance, for minimal problems in high humidity environments. Properties of the epoxy system are listed in Table 2-1.

**Table 2-1** Physical and mechanical properties of the epoxy system

	PR2032 with PH3660	ASTM Method
Mix Ratio	100: 27 By Weight, or 3 to 1 By Volume	PTM&W
Pot Life @ 77 °F	1 hour	D2471
Color	Light Amber	Visual
Mixed Viscosity @ 77 °F ,cps	900 - 950 cps	D2393
Cured Hard ness, Shore D	D 88 Shore D 88 Shore D	D2240
Specific Gravity, grams, cc	1.11	D1475
Density, lb./cu. Inch	0.0401	D792
Specific Volume, cu. in./lb.	25.0	D792
Tensile Strength, psi (1)	9828 psi	D638
Elongation at Break, % (1)	1.90 %	D638
Tensile modulus, psi (1)	418,525 psi/2.885 GPa	D638
Flexural Strength, psi (1)	16,827 psi	D790
Flexural Modulus, psi (1)	462,910 psi	D790
Glass Transition Temp., Tg	196 °F /91 °C	TMA
Thermal Coef. of Expansion Range:	4.3 x 10-5 in./in./°F	D696

## 2.4 Magnetic processing Experiment

Disk-shaped Neodymium 1\*1/2 in" magnets grade 50 from Applied Magnets, Ontario, Canada, were used in this study. The filed strength and direction were measured using the Gaussmeter by Alpha Lab DC Gaussmeter Model1. The magnetic field strength was about 0.5 Tesla. The magnets are magnetized through their thickness. Hence, the field is perpendicular to the magnet flat surface, As shown in Figure 2-5 the containers in which the epoxy to be poured were placed on the top surface of the magnet such that the field is parallel to the container axis.

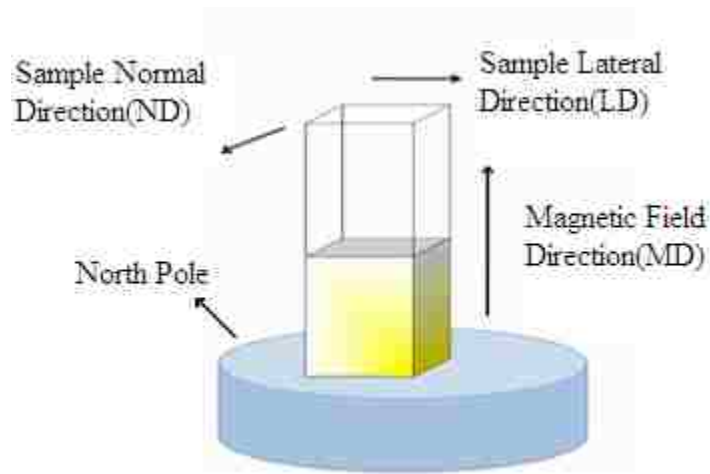


**Figure 2-5:** Schematic of the magnetic processing of the samples. The figure shows the axial and lateral directions of the sample with respect to the direction of the maximum magnetic field.

The resin and the hardener were mixed by a weight ratio of 100:27. Mixture was prepared more than the amount enough to fill the containers. This was done to make sure that the mixture poured in the containers is homogenous, and the mix ratio remains the same when it is being poured.

The mixture was stirred mechanically for 20 seconds to make sure that the resin/hardener mixture was homogenous. Inner sides of the containers were significantly smooth. The specific choice of the container was to get a smooth surface of the sample so

that there would be no need for polishing. Polishing might affect the surface properties as it induces some thermal and mechanical residual effects.

The containers were filled with epoxy up to half their length. This helps facilitate the degassing of any air bubbles in the mix as the polymer gels fairly fast and the degassing occurs from the bottom to the top of the sample. Basically, the shorter the sample the faster it gets degassed. The samples with the magnets underneath, while they are being cured, will be referred to as “magnetically annealed” and the ones without will be called “neat” samples throughout the thesis. A total of four samples for each test were made and put in the vacuum bell jar. The chamber was pumped down to 250 torr.

The heat flux that the samples were receiving while they were getting cured in the vacuum chamber was different from the samples on top of the magnets and the ones on the plastic disc of the bell jar. To be consistent in all steps, two of the magnets were heated up to 500 ° C and held for 15 minutes to completely become demagnetized. The measured field with the use of Gaussmeter was very close to zero. These metal cylinders were placed under neat samples so that the heat flux becomes the same for both magnetically annealed and neat samples.

The epoxy samples were cut using a high precision diamond saw, Isomet 1000, and taken out of the containers. The nanoindentation tests were carried out right after the samples were taken out of the containers to avoid any air exposure. This was to eliminate any effect from the aging or oxidization of the surface to interfere with the measured properties. Further care were taken as the two samples of a kind, either neat or magnetically annealed, were tested as the first and last samples respectively. The other two were tested as the second and third samples. Using the above approach, the average of the properties for neat and magnetically annealed samples will have the same age.

There are many parameters other than the magnetic field effect that can contribute to a difference in the properties of magnetically annealed and neat samples and results in misleading products. We have to keep all these parameters constant to be able to observe the effect of the magnetic annealing. We will discuss these error sources later in chapter 3.

After the samples were glued to the nanoindenter sample holder stub, they were investigated with the means of a level to see if the surface to be tested is parallel to the

stub surface. Some grinding work was needed in some samples to make the two surfaces parallel. Same care was taken before mounting the samples in the WAXD chamber.

None of the sample's surfaces were touched before the indentation tests were done. Any residual stress due to touching of the sample surface might result in different properties.

## **2.5. WAXD Measurements**

It is commonly understood that the amorphous chains segments can have some long-range order. The wide-angle x-ray diffraction is used for the conformation analysis of the amorphous chain segments ordering. Microstructure and alignment was investigated using wide angle X-ray diffraction (WAXD) in a similar way as described before [6, 7]. The X-ray facility used was a Philips X'Pert PW3040 MRD X-ray diffractometer, equipped with a pole figure goniometer, operating at 40 kV and 45 mA, and employing Ni filtered Cu Ka radiation. The machine is located at Materials Science and Engineering building at Georgia Institute of Technology, Atlanta. A standard phase analysis  $2\theta$  scan was performed from  $5^\circ$  to  $55^\circ$  in  $0.02^\circ$  per step for a period of 0.2s per step.

The  $2\theta$  scans for the neat and the magnetically annealed samples at the edge of the sample different epoxy samples at  $\phi = 0^\circ$ , are shown at Figures 2-6-7. There is only one visible halo between  $5^\circ$  to  $55^\circ$ . We have shown the first part of the scan to focus more on the existence of the halo.



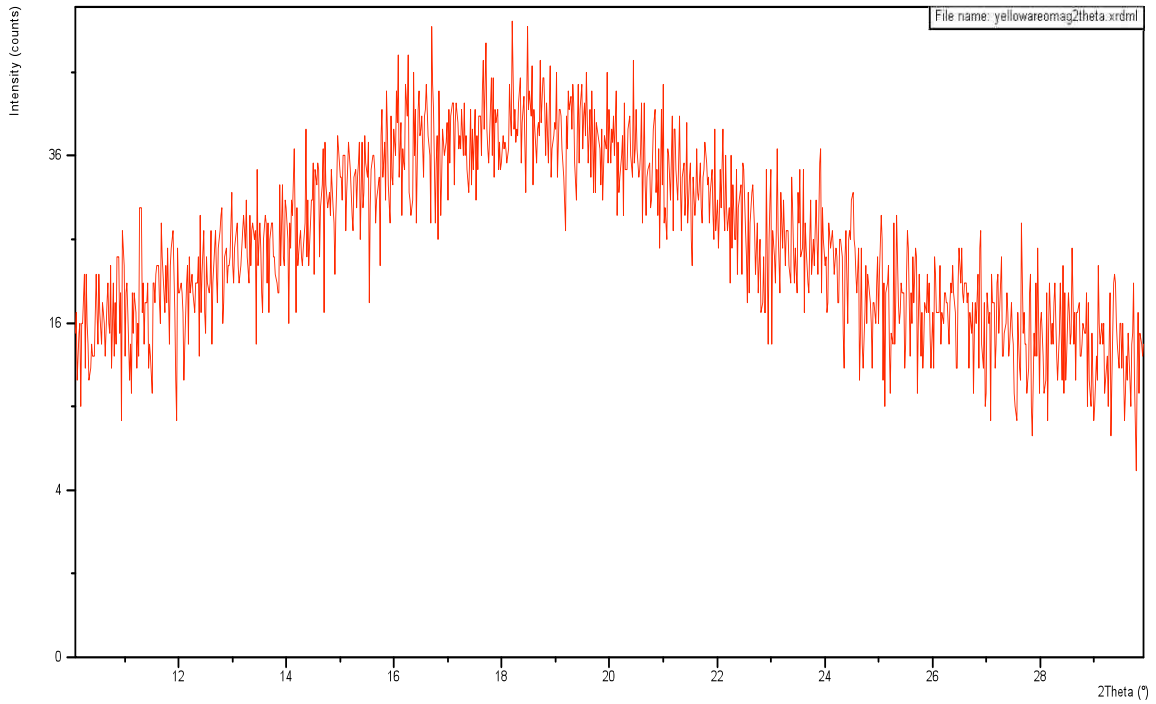


**Figure 2-6** The 2- $\theta$  scan of a magnetically annealed sample. The scan was performed at a point close to the edge of the sample where the magnetic field is maximized.

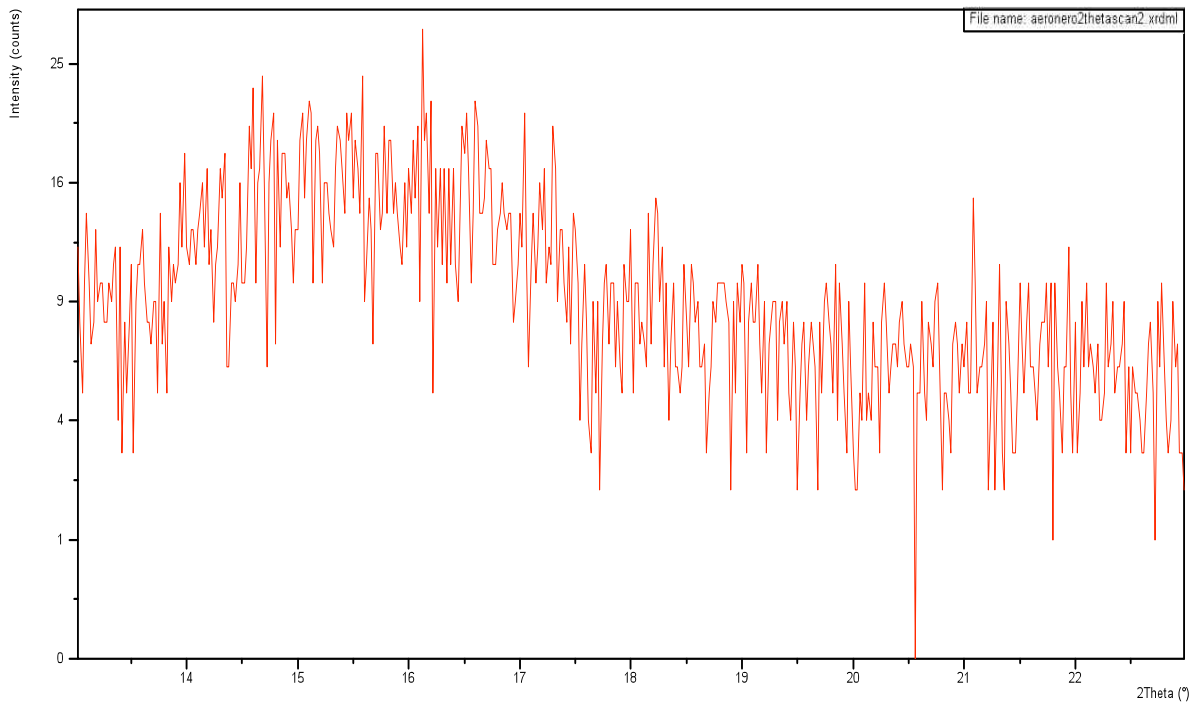


**Figure 2-7** The 2- $\theta$  scan of a neat epoxy sample at the lower edge of the container. The scan was performed at a point close to the edge of the sample where the magnetic field is maximized.

From the 2- $\theta$  scans it is evident that there are no significant peaks that could be attributed to crystalline lamellae, but only a weak diffuse amorphous halo. The degree of crystallinity of epoxy resin is very low.

Most of the macromolecules are in an amorphous region. The analysis of this halo can provide information concerning the structure of the amorphous regions. The position of the halo is at  $2\theta = 19^\circ$ . Thus, the pole figure analysis will be carried out at only  $2\theta = 19^\circ$ .

## 2.6 Texture Results

The reflections from the amorphous halo at  $19^\circ$  were analyzed to determine the alignment of the amorphous halo order. The diffraction data was corrected for geometric defocusing and background X-ray intensity using standard procedures embedded in the preferred orientation software package from Los Alamos (PopLA)[56]. Recalculated experimental pole figures were further normalized to satisfy the following condition:

$$\oint P_{h_i}(y) dy = 4\pi \quad (2-11)$$

where function  $P(y)$  is the volume fraction of the sample for which the halo order normal  $h$  is parallel to the sample direction  $y$  composed by azimuthal angle  $\alpha$  and radial angle  $\beta$ .

The pole figure analysis was carried out on the surface of the samples at different locations L1 and L2 measured along axis parallel to the lateral direction of the magnetic field (LD). The points are 4 mm apart. Similarly pole figures were investigated on the surface of the samples at three different locations along axis parallel to the magnetic field direction (MD); M1 and M2 that are also 4 mm apart. The locations are illustrated in Figure 2-8.

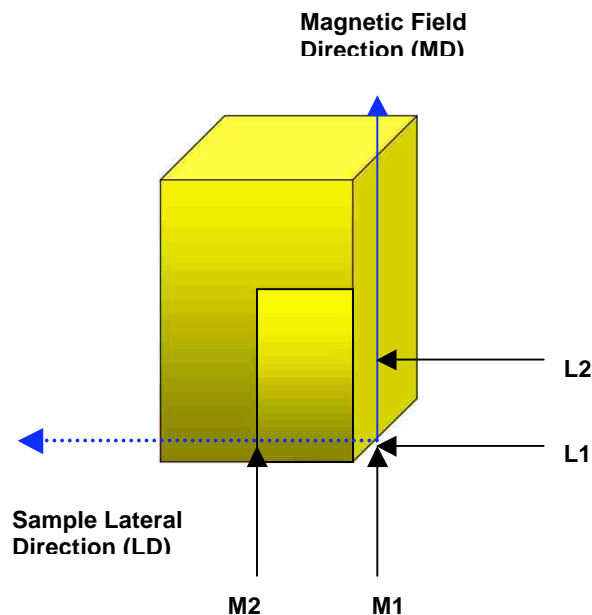


**Figure 2-8:** Schematic illustration of four different locations at which individual pole figures analysis was carried out.

At each designated location in Figure 2-8, incomplete pole figures were obtained from the projections of sample orientation with respect to the incident beam, with azimuthal angle  $\alpha$  varying from  $0^\circ$  to  $85^\circ$  in  $5^\circ$  intervals and radial angle  $\beta$  varying from  $0^\circ$  to  $360^\circ$  in  $5^\circ$  steps. Representative WAXD azimuthal-radial scan for a magnetically annealed sample at location M1 is shown in Figure 2-9. The same azimuthal-radial scan for neat sample at the same location M1 is shown in Figure 2-10. Representative WAXD azimuthal-radial scan for a magnetically annealed sample at location L1 is shown in Figure 2-11. The same azimuthal-radial scan for neat sample at the same location L1 is shown in Figure 2-12.

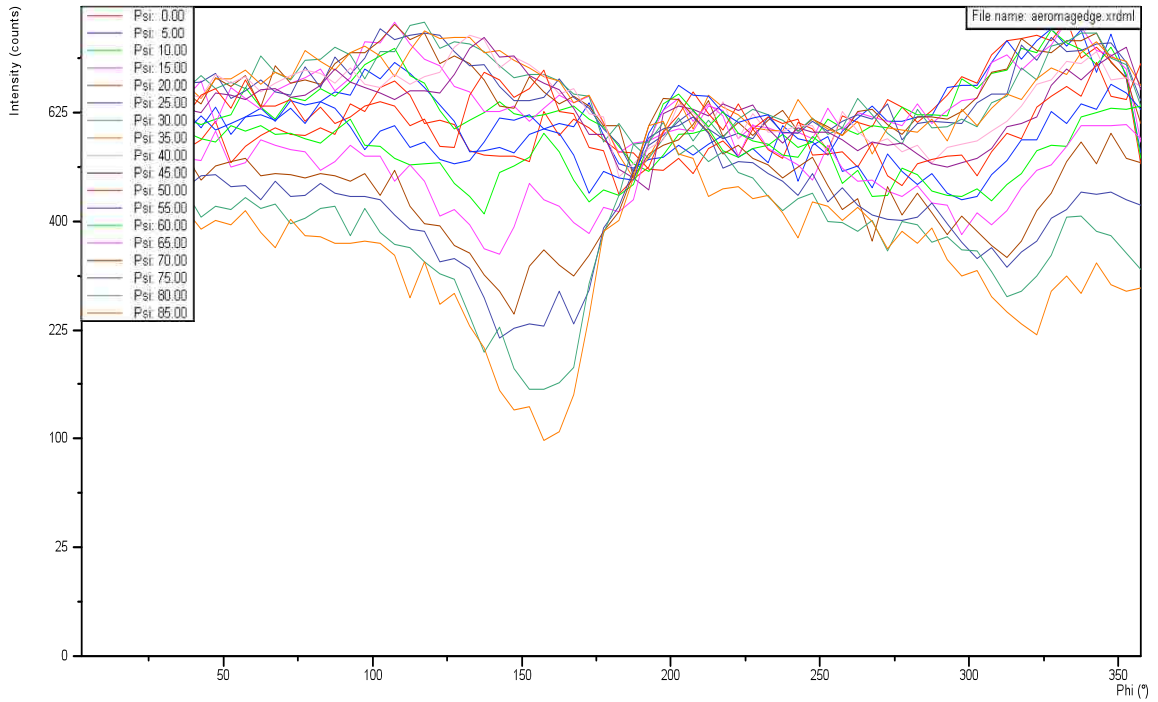


**Figure 2-9:** WAXD azimuthal-radial scan at location M1 for magnetically annealed epoxy sample.

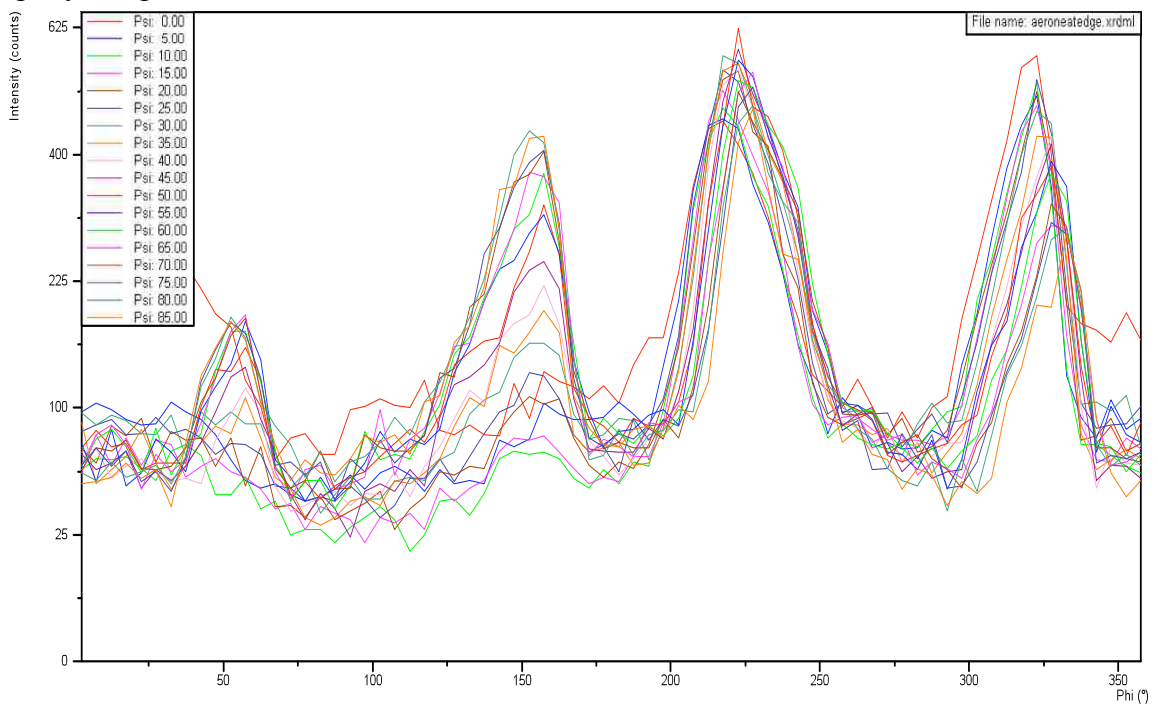


**Figure 2-10:** WAXD Azimuthal-radial scan at location M1 for neat epoxy sample.

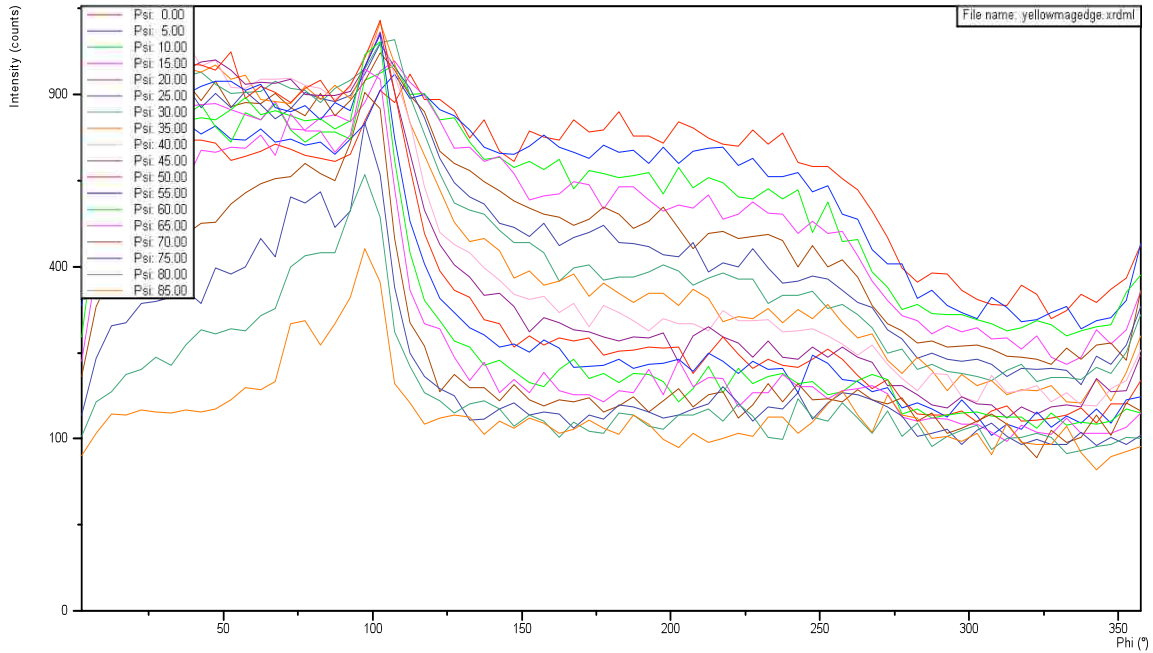


**Figure 2-11:** WAXD azimuthal-radial scan at location L1 for magnetically annealed epoxy sample.

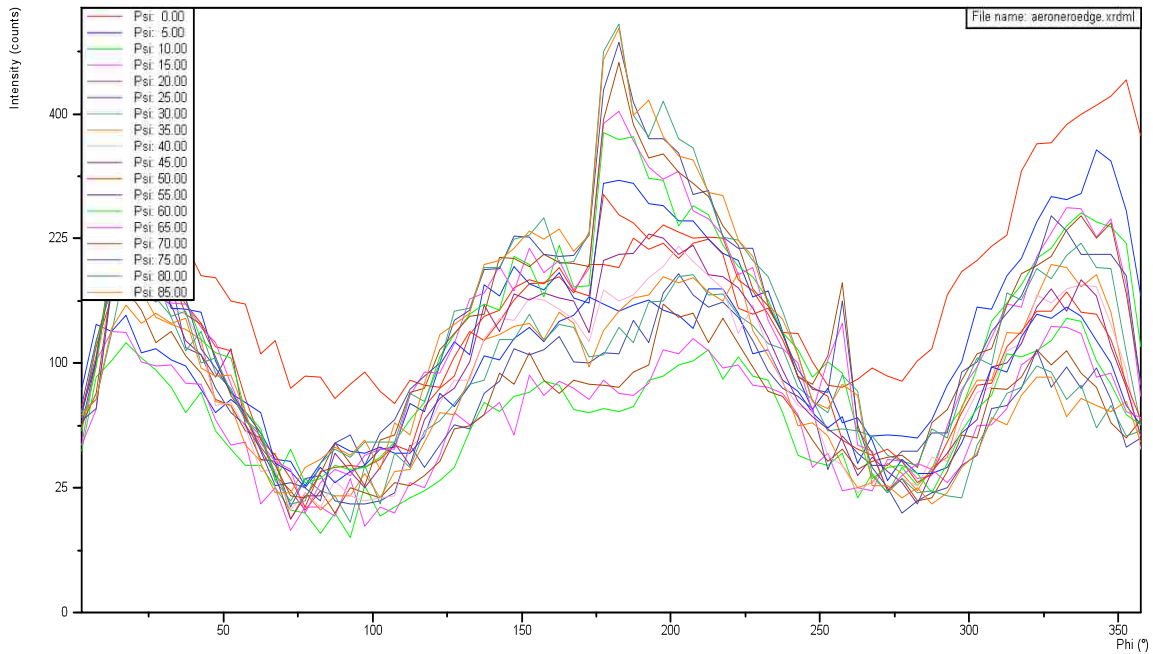
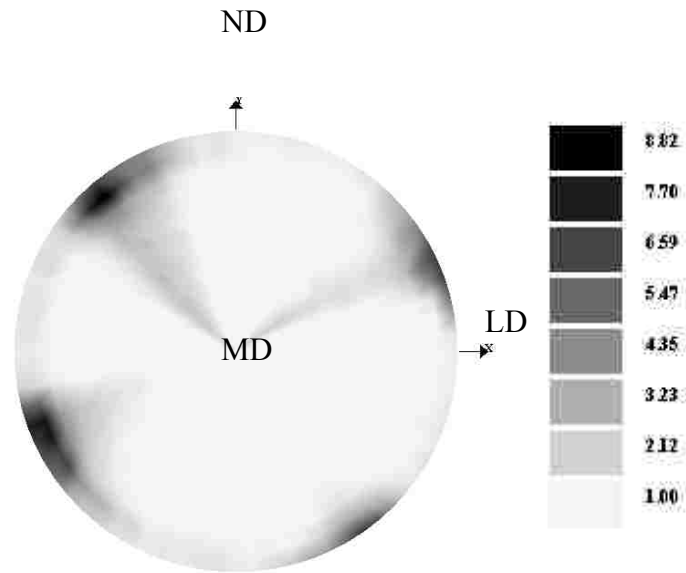
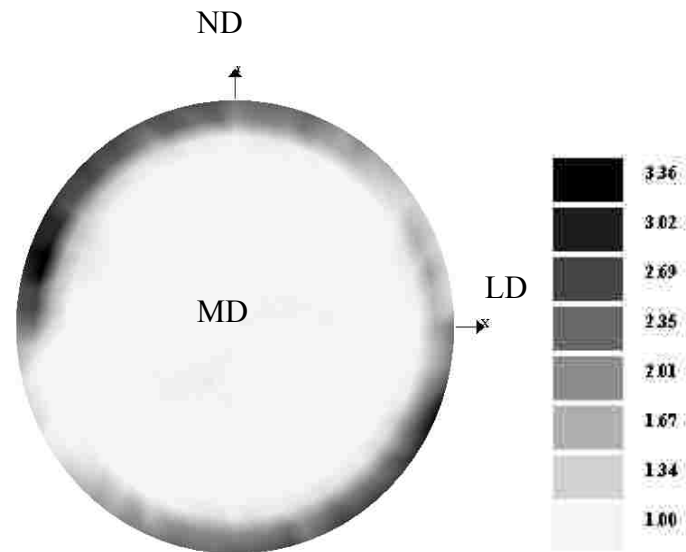


**Figure 2-12:** WAXD Azimuthal-radial scan at location L1 for neat epoxy sample.

From the azimuthal scans, the decrease in the intensity of the peak observed in Figure 2-10 for the neat epoxy as the magnet field is applied is clear in Figure 2-9, and it indicates that the magnetic field had minimized the orientation density along the axial direction of the samples, (MD) that was parallel to the applied magnetic field. The results of the scan along the sample lateral direction (LD) suggest that the magnetic field had forced the amorphous phase to reorient along the transverse direction of magnetic field evident by the intense increase of the intensity from the neat sample at L1, Figure 2-12 to that observed for the magnetically annealed sample at L1 as seen in Figure 2-11. A more practical way to quantify the orientation of the epoxy amorphous halo is to utilize the azimuthal-radial scans to produce the pole figure. Figure 2-13-2-16 shows set of pole figures at the locations M1, M2, L1 and L2, respectively. All the pole figures were corrected against the background intensity and the defocusing according to procedures built in at PopLA.

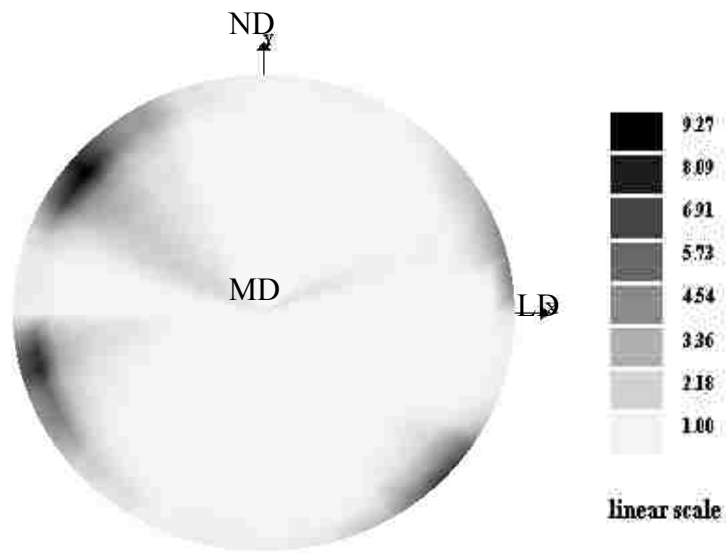


(a)

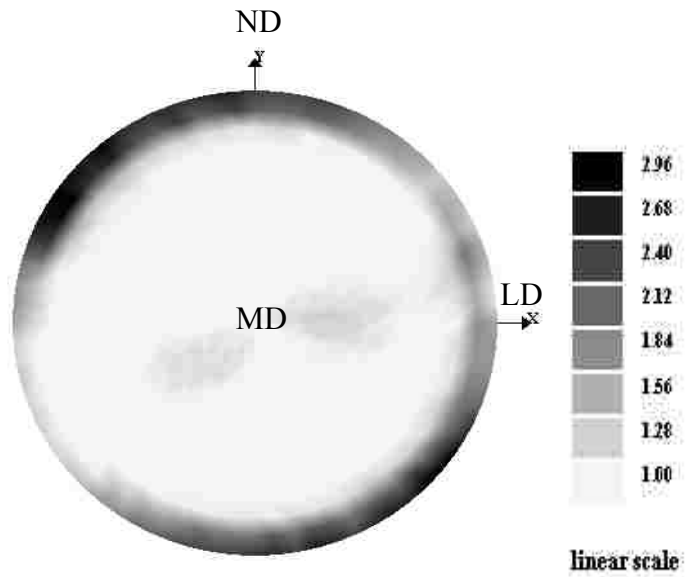


(b)

**Figure 2-13:** Pole figures generated at location M1 for (a) neat epoxy sample and (b) magnetically annealed epoxy.



(a)



(b)

**Figure 2-14:** Pole figures generated at location M2 for (a) neat epoxy sample and (b) magnetically annealed epoxy.



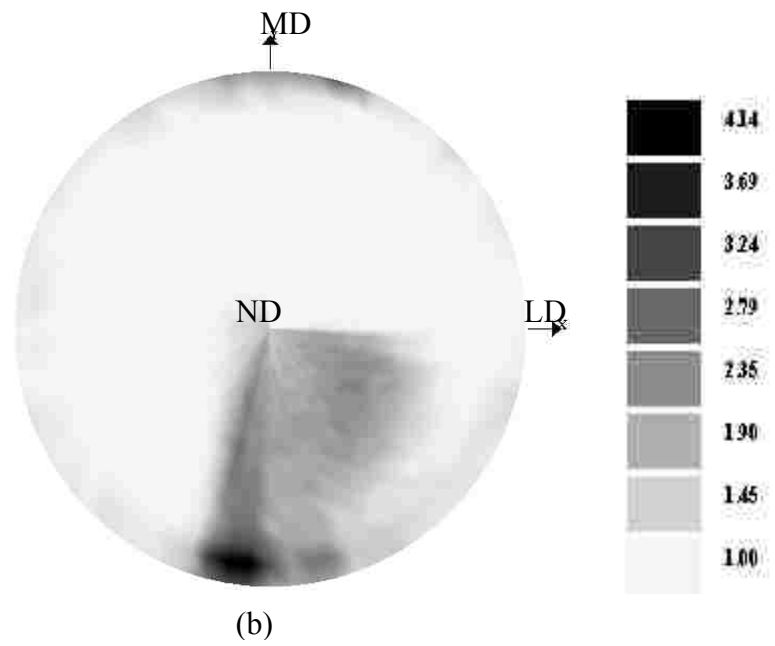
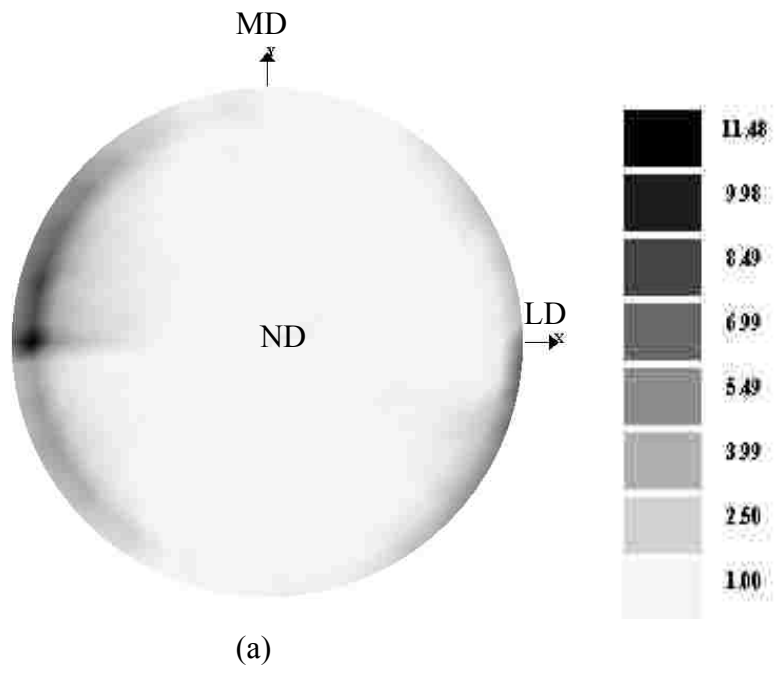


**Figure 2-15:** Pole figures generated at location L1 for (a) neat epoxy sample and (b) magnetically annealed epoxy.

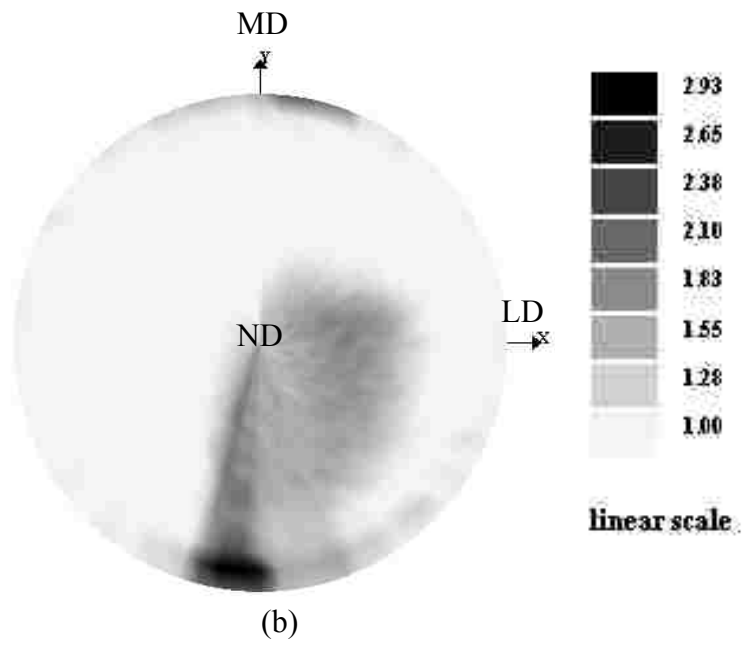
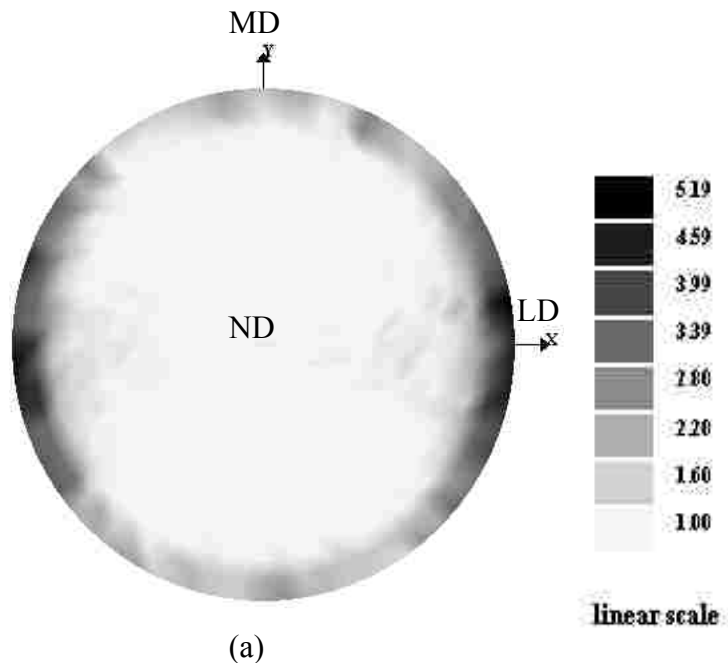


**Figure 2-16:** Pole figures generated at location L2 for (a) neat epoxy sample and (b) Magnetically annealed epoxy.

In all of these pole figures, the color bar shows the normalized raw pole densities plotted in units of time-random distribution in which 1 corresponds to complete random orientation distribution. For Figures 2-13 and 2-14, the intersection of the crosshairs corresponds to the magnetic field direction (MD), while the LD represents the lateral direction, and the ND the normal direction. The maximum pole intensity at location M1 in neat sample (0 Tesla) is 8.82 time- random units which is higher than the 3.36 in the magnetically annealed sample. The high pole intensity of the neat epoxy can be explained in a similar manner to the microstructure build-up in solidifying metals. That is to say the epoxy close to the container bottom -that has a normal MD- will cure first (wall effect) and will be most influenced by the weight of the epoxy along the MD direction. Upon applying the magnetic field, due to the documented diamagnetism of the epoxy [18] it will try to rotate away from the field direction and thus reduce the pole intensity along MD. Actually, the intensity of the pole at MD for the magnetically annealed sample is virtually 1 as shown in Figure 2-13(b), which means that upon magnetic annealing the texture existed along the MD direction; the axial direction of the sample, has disappeared, given place to reorientation of the amorphous epoxy in the planes defined between LD-ND directions.

Similar observations can be seen in locations far from the edge of the samples; at location M2, as shown in Figure 2-14. However, the maximum pole intensities upon magnetically annealing the sample dropped from 3.36 to 2.96, and that is mainly due to the fact that the field intensity fades away upon moving away from the edge of the sample where the field is a maximum. It can be seen far from the field, the pole intensity starts building up along MD, as the weight effect becomes more predominant at the middle of the sample.

For the texture in the lateral direction, separate set of pole figures at locations L1 and L2, shown in Figures 2.15-16. At location L1 for the neat sample the texture arise along L1 again due to the wall effect. Figure 2-15(a). Upon applying the magnetic field, the biaxial reorientation of the amorphous halo decreases the intensity of the pole along LD, and generates a texture in new planes enclosed between the LD-ND directions as shown in Figure 2-15(b). Moving away along the LD to point L2, we still can observe

the biaxial reorientation induced by the magnetic field in the LD-ND with lesser pole intensity; max intensity 2.94, in Figure 2-16(b).

From the pole figure analysis one can conclude that a neat epoxy sample will have a texture along the walls it cures on; LD and MD. Upon application of the magnetic field, biaxial reorientation of the amorphous halo will take place on planes transverse to the magnetic field.

The above mentioned two-dimensional orientation; in-plane orientations, are in good agreement with our previous studies of the same epoxy resin system cured under much higher magnetic fields (15 and 25 Tesla) magnetic fields in which it was found that the presence of the magnetic field during the cure reaction aligned the molecules along the applied field [49], shown in Figure 2-17.

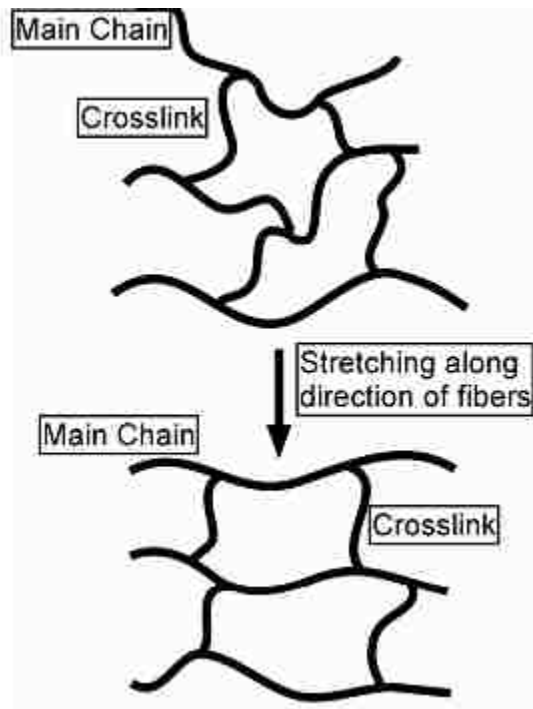


**Figure 2-17:** The two-dimensional stretching effect a magnetic field exerts on the main chains and crosslinks of an epoxy.

## **CHAPTER 3: NANOINDENTATION TESTS AT AMBIENT AND ELEVATED TEMPERATURES**

### **3.1 The Nanotest System**

The Nano Test 600 is a pendulum based nanoindentation machine developed by Micro Materials Ltd. United Kingdom. The system has 3 separate modules that consist of indentation, scanning (scratch) and impact. All three modules can be used in conjunction with the low load head which is 0.1-800 mN.

There are a wide range of testing options which the system provides: Spherical indentation, pin-on-disc wear testing, continuous contact compliance (CCC) measurement, high temperature testing, wet-stage testing, AFM scanning, nano-positioning, nanoscratch, friction and impact/impulse testing. Transverse sample movements during loading enable scanning measurements (scratch testing, fatigue and wear testing). Sample oscillation at constant load is used for impact testing, contact fatigue testing, nano-positioning and dynamic testing.

The system is placed inside a thermally insulated cabinet. This cabinet serves to reduce air turbulence that would upset the pendulum and to provide a thermally controlled environment and also to provide soundproofing to reduce acoustic disturbances. The system at UNM has a noise level with a standard deviation of 0.5 mV while the reference sample is in contact with the Berkovich tip.

At the heart of the NanoTest system is a pendulum that can rotate on a frictionless pivot, Figure 3-1. A coil is mounted at the top of the pendulum; with a coil current present, the coil is attracted towards a permanent magnet, producing motion of the diamond tip towards the sample and into the sample surface. The displacement of the diamond tip is measured by means of a parallel plate capacitor. One plate of which is attached to the diamond holder. When the diamond moves, the capacitance changes, and this is measured by means of a capacitance bridge. The capacitance bridge unit is located close to the measuring capacitor in order to minimize stray capacitance effects.

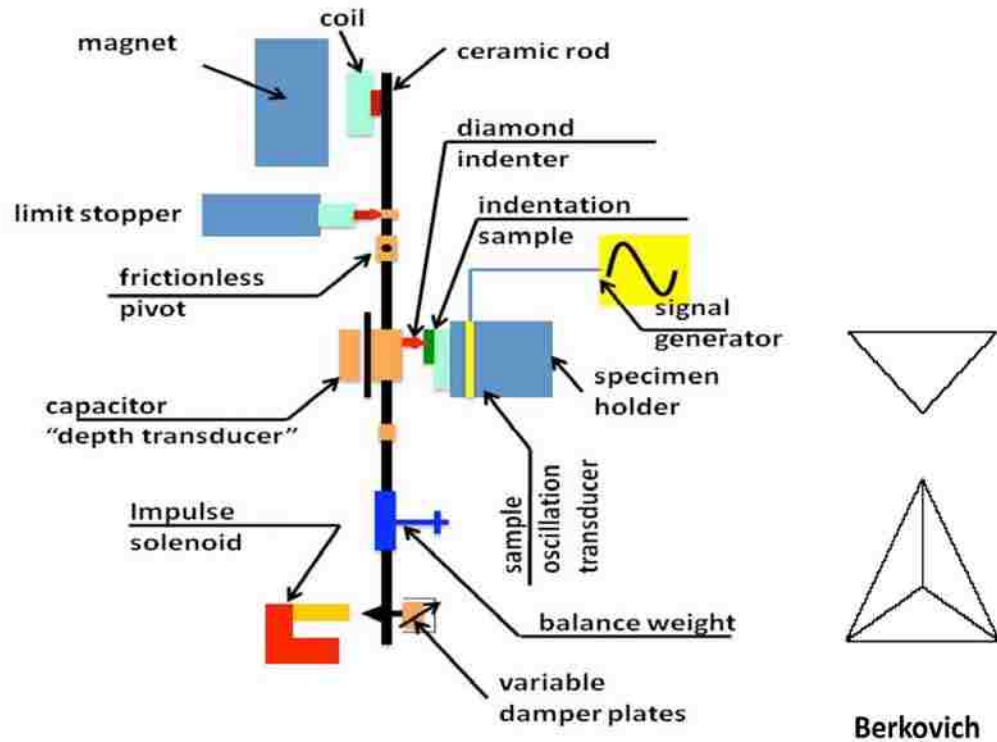


**Figure 3-1:** Schematic of the NanoTest with two different views of the Berkovich indenter (Micro Materials Ltd.)

Sample positioning displacement is achieved by means of three DC motors driving micrometer stages in an XYZ configuration. The motor control electronics consists of a motherboard containing three power modules, an IEEE interface module and a backlash control board. The motor power supply is driven by the controllers through visual interface of the system software in the computer, with motor positioning obtained by means of magnetic encoders. The motor control board communicates with the system computer via the IEEE bus. The limit stop defines the maximum outward movement of the diamond, and also the operating orientation of the pendulum, when a load is applied. Its position is manually adjusted with a micrometer. The equilibrium position of the pendulum, with zero load current, is adjusted with balance weights which are movable along both the horizontal and vertical axes [57].

The theoretical resolutions of the UNM system are a load resolution of 1 nN and a depth resolution of 0.004 nm as given by Micro Materials Ltd. at the time of purchase.

Due to the location's environmental factors (vibration from other labs, slamming of doors on the same floor, etc.) the machine can not actually reach this level of accuracy. The machine has a variety of calibrations, some of which are more often performed than others. Some of these are:

- *Load calibration* – Establishes the forces that can be applied at the diamond tip during a measurement
- *Depth calibration* – Relates the change in capacitance to a known distance moved by a sample in contact with the pendulum
- *Frame Compliance* – Corrects for “flexibility” in the structure of the machine
- *Microscope* – Includes a calibration for the distance from the indenter tip to the focal plane and a calibration to position the sample for precisely placed indentations

There are two different methods for accurately determining the machine/frame compliance (FC) of the NanoTest system. First method is an indirect method using a reference sample of known modulus; fused silica. The second method is the direct compliance measurement method. One needs to know the exact area of impression of the indenter at any depth to be able to do the analysis using this method, while the indirect method assumes an ideal Berkovich shape for high loads/depths. Knowing the properties of the reference sample, fused silica in our study, some maximum load indentations, 200 mN for example, are carried out on the reference sample from which the frame compliance is calculated.

The direct method uses a rigid pin to solder the stage to the indenter. A simple load ramp-up is done and the only compliance due to the machine flexibility is measured. For our machine a compliance of 0.51 nm/mN was measured using both methods. From the measured data the contact compliance can be determined and then the sample compliance is obtained from:

$$\text{Total (measured) compliance (Ct)} = \text{contact compliance (C)} + \text{Machine/frame compliance (Cf)}$$

When the sample compliance is small (high modulus sample) the machine compliance makes up an appreciable fraction of the total measured deformation and so small errors in

the machine compliance can affect the accuracy of the sample modulus determination. In the case of viscoelastic materials which are considered soft compared to metals, the frame compliance does not play a critical role.

### **3.2 Nanoindentation Data Analysis**

The Nano Test software uses a method developed by Oliver and Pharr for analysis [58]. This method uses the load vs. displacement curves to determine the hardness and elastic modulus of a given material. All the indentations on the polymer samples were carried out using a Berkovich indenter. A cross section of the Berkovich indenter is shown in Figure 3-2 (b). A Berkovich tip is a three sided pyramid which is geometrically self similar. It has a flat profile with a total included angle of 142.3 degrees and a half angle of 65.35 degrees. A typical indentation curve is shown in Figure 3-2(a). This figure also shows the values needed to do the analysis described by the Oliver and Pharr method.

There are three experimental values that are critical to find the hardness and elastic modulus. These are the peak load ( $P_{\max}$ ), the depth at peak load ( $h_{\max}$ ), and the initial unloading contact stiffness (S).



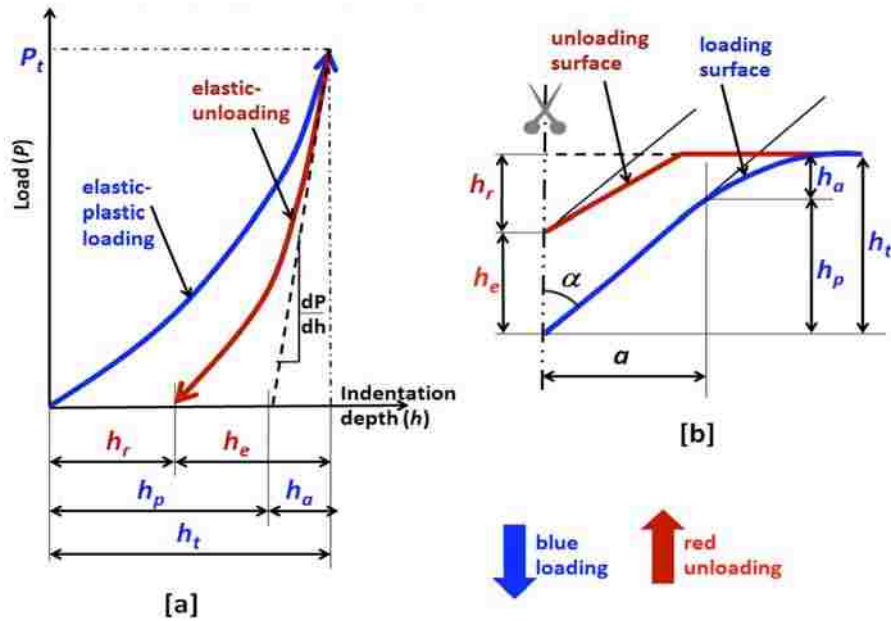


**Figure 3-2:** (a) Typical loading vs. indenter displacement curve (b) cross-section of a Berkovich indenter trace in the sample.

The software analysis begins by fitting the unloading curve from 100% to 40% of  $P_{max}$ . This is achieved by fitting the polynomial:

$$P = \alpha(h - h_r)^m \quad (3.1)$$

where  $\alpha$ ,  $m$ , are constants determined by the least squares fit and  $h_r$  is the displacement when  $P=0$ . By differentiating this equation the contact stiffness can be derived.

$$S = \frac{dP}{dh} = \alpha m (h_t - h_r)^{m-1} \quad (3.2)$$

Once  $S$  is found the contact depth can then be calculated using:

$$h_p = h_t - \epsilon \frac{P_t}{S} \quad (3.3)$$

where  $\varepsilon$  is an experimentally determined correction factor for the indenter used ( $\varepsilon = 0.75$  for a Berkovich indenter tip.  $\varepsilon = 1.0$  for a spherical indenter). The software then uses a truncated version of Oliver and Pharr's area function

$$A(h_p) = 24.5h_p^2 + f(h_p) \quad (3.4)$$

Here  $f(h_p)$  is a fifth order polynomial, the coefficients of which are determined from a graph obtained from indentations done on the fused silica. This curve is called the diamond area function or DAF for short. As shown in figure 3-3 the curve relates the contact area under the tip to the plastic depth. These indentations are carried out in a full depth range up to about one micron. For depths deeper than one micron, we assume an ideal Berkovich shape which is in good agreement with the tests done on the fused silica.

Knowing the frame compliance and the properties of the reference sample, fused silica in our study, we are able to find the projected contact area of the indenter tip at  $h_p$ . Once the stiffness and the projected area are obtained, the software calculates the effective modulus using

$$E_{eff} = \left( \frac{\sqrt{\pi}}{2} \right) \left( \frac{1}{\sqrt{A(h_p)}} \right) \left( \frac{1}{\frac{1}{S} - C_f} \right) \quad (3.5)$$

$C_f$  is the frame compliance factor of the Nano Test system that is found through machine calibrations. The hardness to the sample can be computed using

$$H = \frac{P_{max}}{A(h_p)} \quad (3.6)$$

where  $A$  is the contact area of the indenter. Hence, the reduced modulus can be determined from the contact stiffness of the material which can be determined from the slope of the unloading curve as shown in Figure 3-2(a).

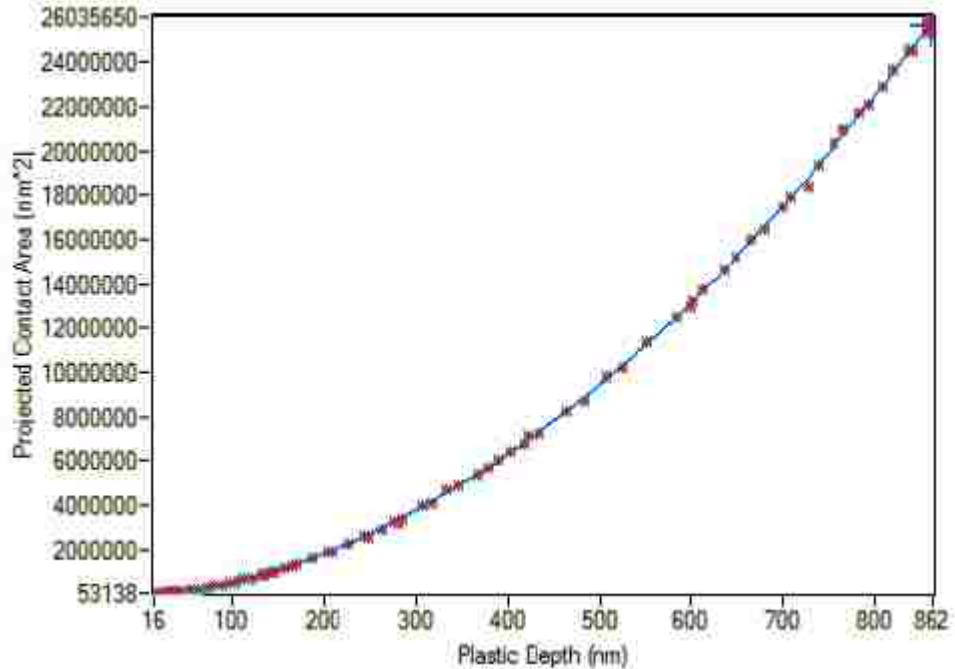


**Figure 3-3:** DAF for the Berkovich tip used in this study

The loading setup is shown in Figure 3-4. A representative nanoindentation load vs. depth curve on one of the polymer samples of our study is shown in Figure 3-5. As illustrated, this curve is different from the loading/unloading curve of Figure 3-2(a).

The main idea of the Oliver-Pharr analysis is based on the fact that the unloading part of the nanoindentation is largely elastic. This enables us to use the slope of this, usually, linear part of the curve to calculate the effective modulus of the tested material. For some metals and most of the non-metallic materials deformations under the tip are not just elastic-plastic but viscoelastic/plastic deformations occur too. To eliminate the viscoelastic/plastic effect, which usually results in a nonlinear unloading curve, the sample is held at the maximum load. The sample also can be unloaded faster to diminish any of the time dependent properties contribution to the unloading part of the indentation.

The holding time depends on the material to be tested and can vary from 30 seconds for metals to 200 seconds or more for viscoelastic materials. By holding the sample at maximum load we let the sample to creep [59]. This time period will allow the time dependent behavior of the polymer to happen at a slower pace as shown in Figure 3-6.

Creep of the sample at maximum load can be seen in Figure 3-6. For the epoxy in our study a time period of 80 seconds was chosen to bring the creep depth vs. time curve to a constant slope. The first sharp rise stage of the creep should be avoided as the viscoelastic behaviors are still happening at a fast pace.

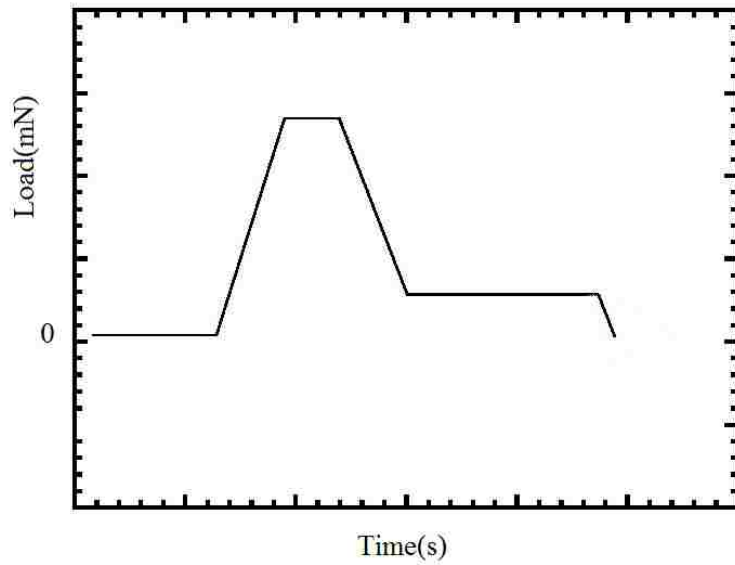


**Figure 3-4:** Schematic of Loading/Unloading vs. time for an indentation

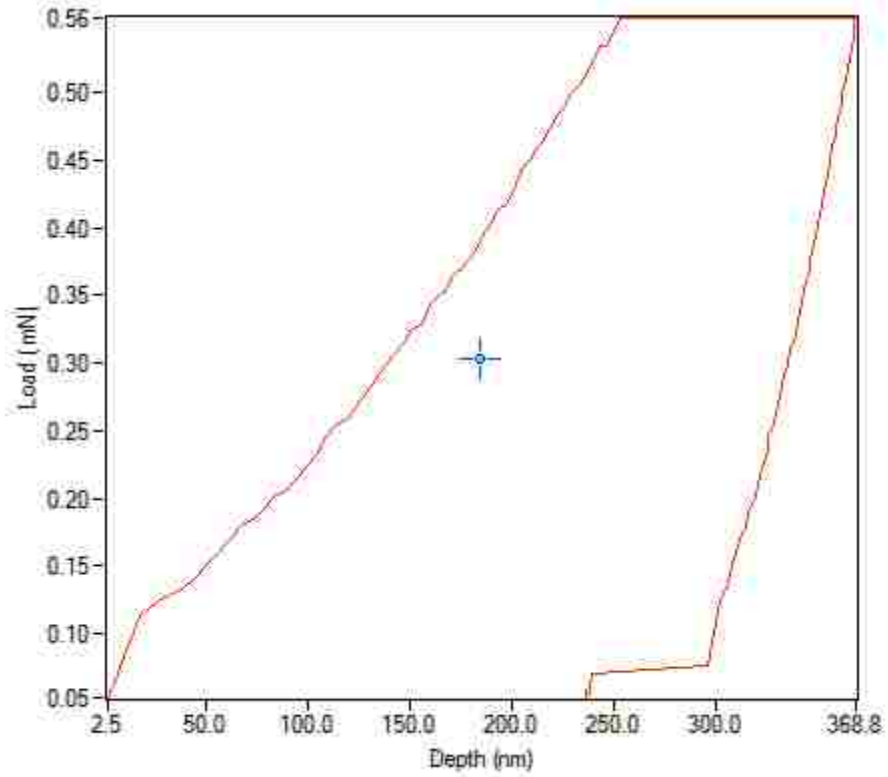


**Figure 3-5:** A representative indentation curve on the polymer of the current study with creep and thermal drift data collected

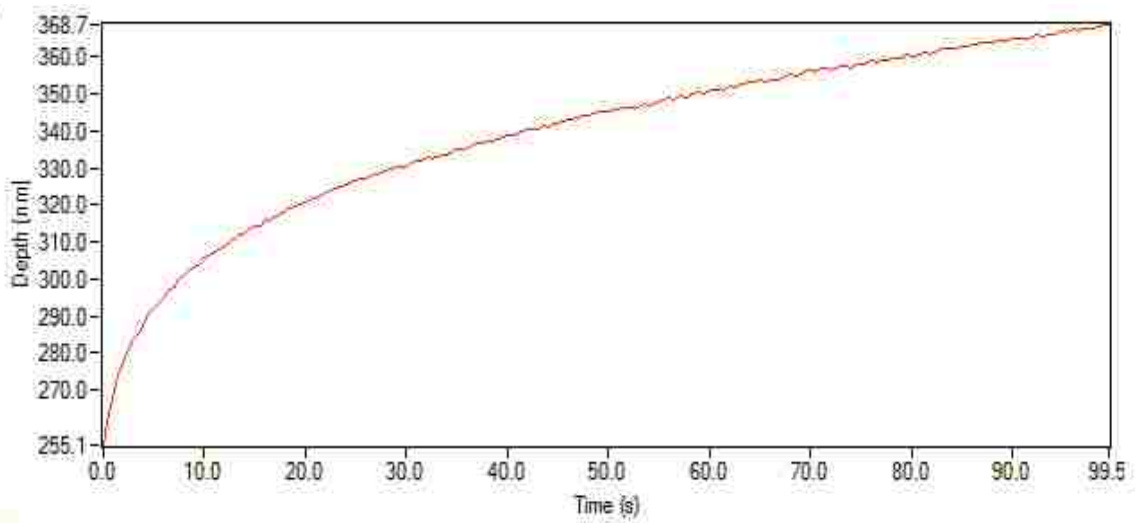


**Figure 3-6:** Creep of the sample at maximum load

Thermal drift data, which is usually collected at the last part of the unloading for the polymer of our study, is shown in Figure 3-7. The second half of the data is used for thermal drift corrections. Creep is mostly due to viscoelastic behavior of the material at the first half. The creep continues due to the thermal expansions of the indenter and the sample. The actual data can be corrected from the data collected at low loads where viscoelastic effects are weak. As can be seen in Figure 3-7 the cabinet temperature has stayed fairly constant and the thermal drift can be ignored [59].

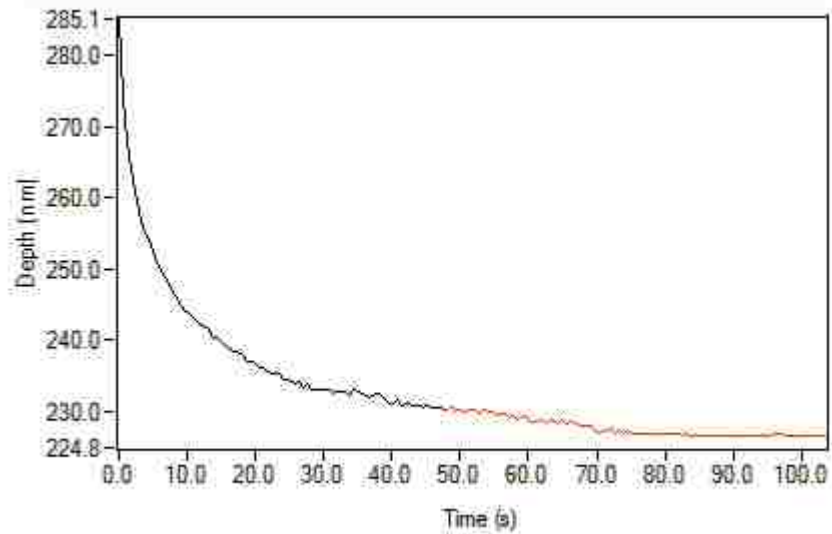


**Figure 3-7:** Thermal drift data collected at 90% of unloading

### **Elastic and plastic work:**

Similar to the macroscale tensile stress-strain curves, the area under the nanoindentation curve is qualitatively representative of the material toughness. Although it is not quantitatively in agreement with the bulk toughness but can be used to compare different materials toughness at the same indentation depth. What is presented here is just the plastic plus elastic work exerted by the indenter on the sample. These quantities are not calculated per volume of the material, hence, they cannot be used to compare two toughnesses at different depths. Thus in the current study, one can only qualitatively compare the toughness of the samples.

The elastic and plastic works, as shown in Figure 3-8, can be calculated using:

$$W_E = \int_{h_r}^{h_i} Pdh \quad (3.7)$$

$$W_P = \int_0^{h_i} Pdh - W_E \quad (3.8)$$

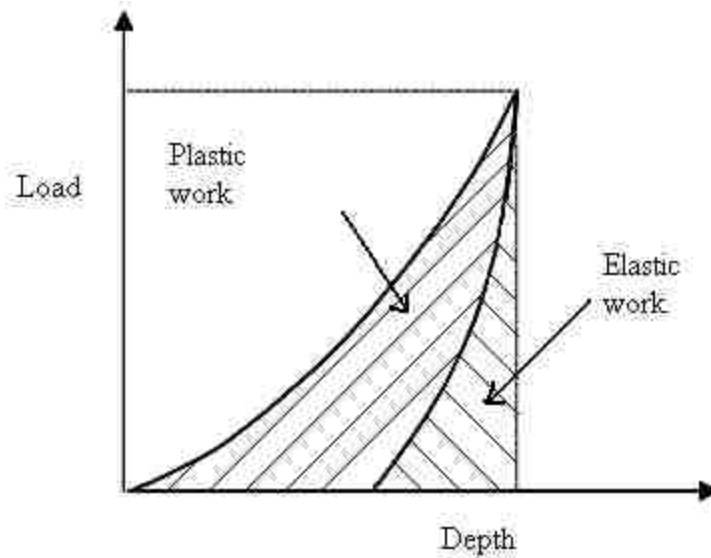


**Figure 3-8:** Plastic and Elastic work for an indentation

### 3.3 Nanoindentation of Viscoelastic Materials

Nanoindentation testing for extracting mechanical properties of metallic materials has become so common and widely used by experts. However, polymeric materials create significant challenges for measuring the modulus ( $E$ ) accurately using indentation testing [60].

First, many polymers are so soft that the material response cannot be measured at all with depth sensing indentation devices because the system compliances are too low. Even for stiffer polymers ( $E > 1$  GPa), producing indents with both lateral and depth dimensions much less than  $1\mu\text{m}$  is difficult [60, 61].

There has been significant effort in the field of indentation of viscoelastic/plastic materials [62]. Beside approaches typically used for metals viscoelastic/plastic

constitutive behavior, there is not a unique model or interpretation for polymeric materials that all the viscoelastic polymeric materials can be described with.

The effect of different indenter shapes being spherical [63-65], Berkovich, canonical [66] and the effective indenter shape [67, 68] have been investigated both analytically and experimentally[66]. It was shown that the behavior of the material is different depending on the shape of the indenter [69, 70].

Less plastic deformation occurs when the spherical or blunt tips are used while plastic deformations are dominant in the case of sharp indentations [66, 68].

Stress-strain curve for viscoelastic material can be derived from indentation curves done either with spherical or sharp indenters[69]. Several modeling techniques have been utilized and some reliable procedures are available for separate extractions of elastic and time dependent properties of the materials [67]. Different loading/unloading histories are used to make the elastic, plastic and viscous behaviors distinguishable [63, 64, 68, 71-73].

It is common that the properties, which are derived from indentation test at micro/nano scale, might not fully agree with bulk properties of inhomogeneous materials such as epoxies. This is mainly because we are performing the test on the surface of the material which might have different properties than the core due to several processing factors.

Variety of finite element method (numerical)[67], dashpot-spring modeling (analytical)[65, 68], and experimental works have been utilized to relate the nanoindentation curve to viscous and non-viscous properties of the polymeric materials.

In our study we tried to eliminate any time-dependent behavior by holding the sample at maximum load for longer times and unloading at faster paces [71]. The main interest of this chapter is to show the mechanical properties for magnetically annealed samples by utilizing nanoindentation testing.

### **3.4 Nanoindentation Results**

Nanoindentation tests were carried out along both lateral (LD) and axial directions (MD). Axial and lateral directions were defined earlier as in Figure 2-5.



Nanoindentations were carried out at maximum load levels of 1, 2 and 5 mN respectively to enable the observation of any load dependency of the mechanical properties. The loading rate was set to 0.05 mN/s. The Unloading rate was set to 0.1 mN/s. These rates are based on the fact that time-dependent behaviors are strongly present. Upon reaching the value of the designated maximum loads the samples were allowed to creep for 80s before unloading. A second hold period, as mentioned before, (after unloading to a low load level) can be carried out to account for thermal drift. We did not collect any thermal drift data in this study as discussed earlier in the chapter.

A minimum distance of 100  $\mu\text{m}$  was set between each indent. For each sample, a total of 5 nanoindentation tests at each load were carried out to calculate the hardness, modulus and elastic/plastic work values. Figures 3-9 and 3-10 show three loading/unloading hysteresis series for two epoxy samples processed with and without magnetic fields, respectively.

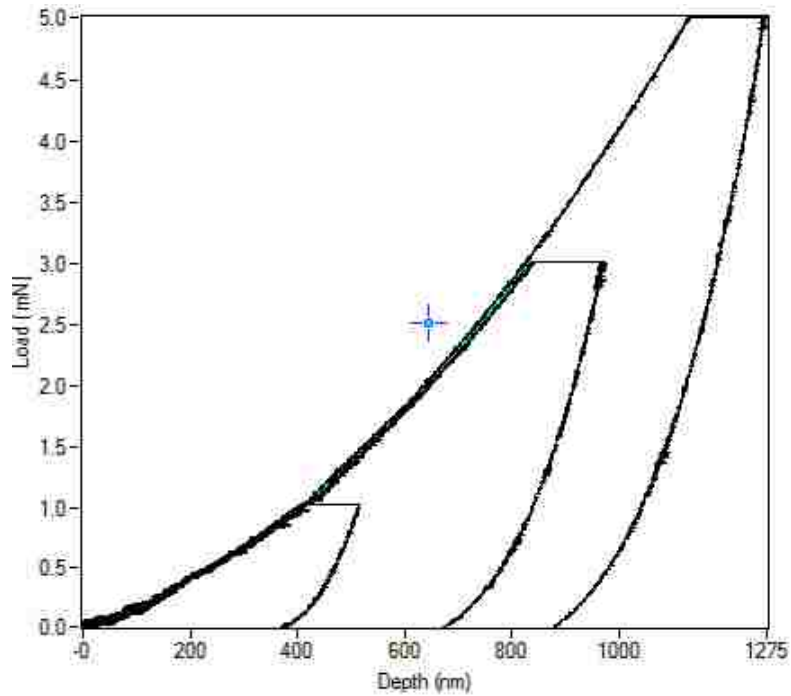


**Figure 3-9:** Nanoindentation load–displacement hysteresis of a sample that was magnetically processed. The maximum loads applied were 1, 3 and 5 mN, respectively, at a loading rate of 0.05 mN/sec and unloading rate of 0.1 mN/sec.

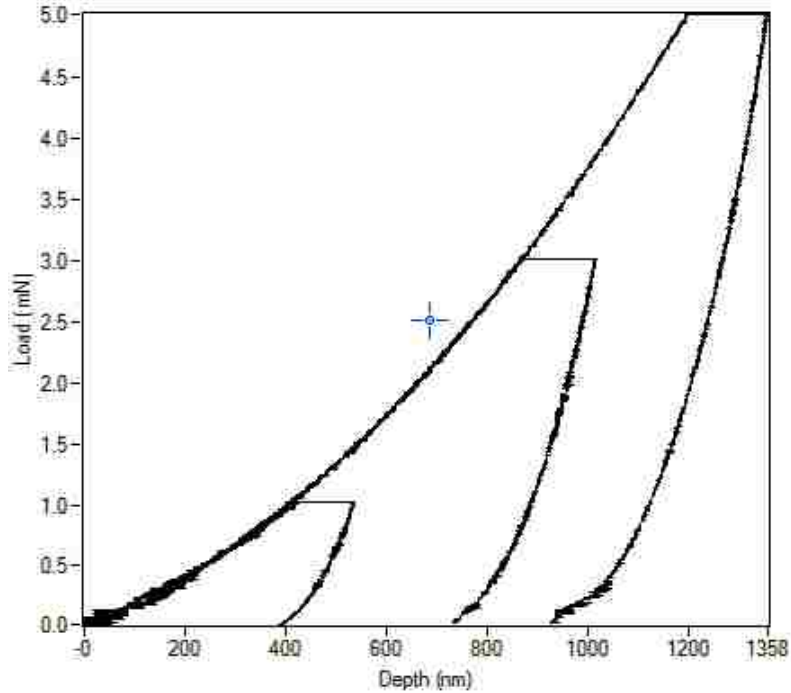


**Figure 3-10:** Nanoindentation load–displacement hysteresis of a sample that was not magnetically processed. The maximum loads applied were 1, 3 and 5 mN, respectively, at a loading rate of 0.05mN/sec and unloading rate of 0.1 mN/sec.

The results of the nanoindentation tests along the axial and lateral directions are summarized in Table 3-1. It is apparent from Table 3-1 that the magnetically induced orientation enhanced the modulus in both axial and transverse direction due to the biaxial orientation of the chains explained in Figure 2-17. However, little change was observed between the neat and magnetically annealed samples at higher maximum loads- and thus at higher indentation depths- as the magnetic field effects fades away. To some extent the little improvement was observed for the hardness. Also the magnetic field seems to embrittle the samples evident by the decrease in the plastic plus elastic work along the both the transverse and axial orientation of magnetic field.

**Table 3-1** Mechanical properties for magnetically annealed and neat samples in both lateral and axial directions

	Load (mN)	Axial Direction			Lateral Direction		
		With Magnet	No Magnet	% change	With Magnet	No Magnet	% change
<b>Reduced Modulus (GPa)</b>	1	4.579 ± 0.171	4.338±0.172	5.6	4.488±0.172	4.358±0.178	3
	3	4.215±0.112	4.126±0.106	2.2	4.023±0.034	3.821±0.087	5.3
	5	4.026±0.140	4.041±0.075	-0.4	3.901±0.053	3.655±0.077	6.7
<b>Hardness (GPa)</b>	1	0.2182±0.0229	0.2147±0.0097	1.6	0.1899±0.0032	0.1957±0.0165	-3
	3	0.1965±0.0128	0.1946±0.0063	0.1	0.1766±0.0029	0.1656±0.0074	6.6
	5	0.1886±0.0133	0.1906±0.0055	-1	0.1713±0.0043	0.1607±0.0064	6.6
<b>Elastic+ Plastic work(nJ)</b>	1	0.26±0.02	0.26±0.00	0	0.29±0.00	0.30±0.00	-3.3
	3	1.27±0.04	1.29±0.02	-1.6	1.392±0.00	1.462±0.02	-4.8
	5	2.69±0.07	2.71±0.04	-0.7	2.88±0.03	3.01±0.04	-4.3

### 3.5 Uncertainties in Nanoindentation Measurements for Viscoelastic Materials

For metals, nanoindentation test at shallow depths of hundreds of nanometers reveals that measured hardness increases strongly with decreasing indent depth, which is frequently referred to as the size effect [74]. Similar to metals, the hardness of many polymers increases with decreasing indentation depths at different depth ranges from several microns down to several nanometers. Such phenomenon for metals is commonly due to geometrically necessary dislocation densities. The same explanation cannot be applied to polymers. Nanoindentation size effects in polymers can be related to Frank elasticity which arises from bending distortions of the polymer chains and their interactions [75]. It can be shown that size effects are due to the finite bending stiffness of the polymer chains and their interactions.[76]

Three other major sources of errors are (1) the angle at which the sample is mounted on the stub (2) the age of the sample (3) surface roughness. We observed that the properties for a sample mounted at an angle of 7 degrees are 5-7% different from the properties measured when the sample is mounted parallel to the stub.

As discussed before in chapter 2, aeropoly cures at room temperature within 24 hours. Some nanoindentation tests were performed on the polymer samples and we observed that after 4 days of casting, the properties remain constant to an acceptable amount. The first two days after the sample has been made, there was a sharp change in properties of the sample as the time passes by and indicates that the sample was still curing.

We let the samples cure for 4 days. Then we took them out of the containers and did the testing. We did not let the sample surface be exposed to air; hence we do not have any oxide layer on top of the sample surface. It can also be seen that the loading part of the indentation curve looks normal and there is no change in the trend that the curve follows as indenter penetrates through the surface.

Roughness can contribute to a change in the measured mechanical properties at the surface of the material. According to the atomic force microscopy (AFM) scans we performed on the polymer surface, a peak-to-peak roughness of less than 100 nm was observed. Tremendous care was taken to make sure that the only difference in properties is due to the magnetic field effect and none of the above sources are present. Consistency was observed through all making and testing of the samples.

Figures 3-11 and 3-12 show AFM pictures along with a cross section of an indentation. The pile-up phenomenon which results in an overestimation of the mechanical properties[77] was observed in the cross sectional view of the indentation in Figure 3-12.

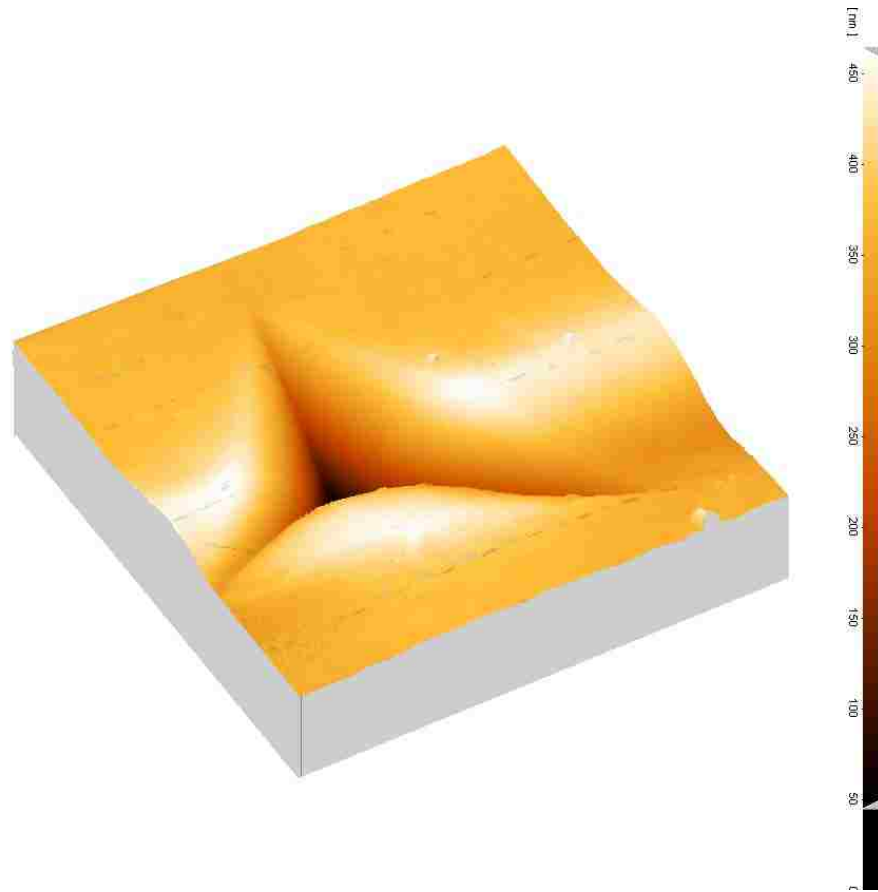


**Figure 3-11:** 3-D AFM scan of an indentation

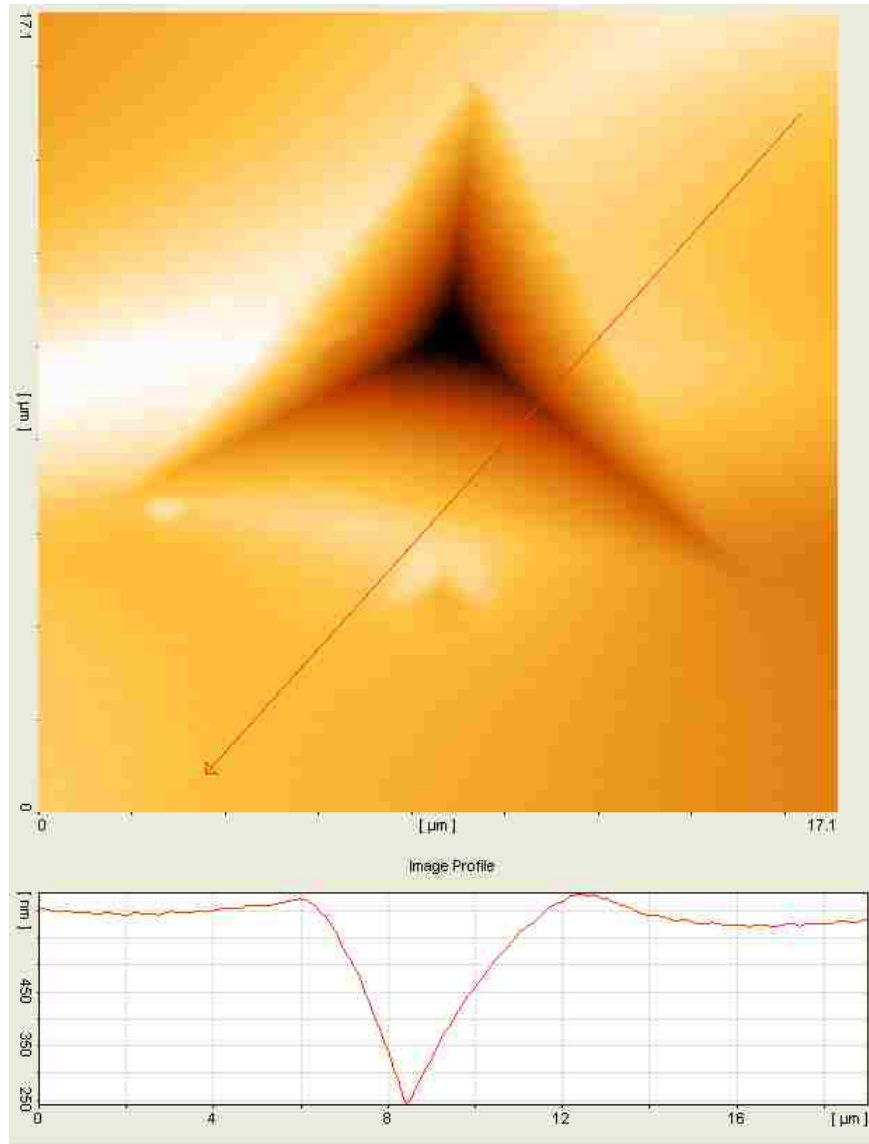


**Figure 3-12:** 2-D AFM scan of an indentation with the cross section showing the pile up

### 3.6 Hot Stage (HS) Nanoindentation

Since all the mechanical properties are temperature dependant, nanoscale measurements at elevated temperature are of high importance. The NanoTest 600 has the hot stage (HS) indentation module which allows to measure properties at temperatures as

high as 500 °C [78, 79]. Both indenter and sample are heated to the desired temperature then a regular is carried out.

Polymeric materials have mechanical properties that are strongly time and temperature dependent. High temperature properties of epoxies are of high importance because the viscoelastic behavior is highly temperature-dependant and dominates as we increase the temperature [80-82].

Adding the testing under elevated temperature capability to a nanoindenter provides a route for testing directly at operating/processing temperature. In addition the glass transition temperature of polymers and especially polymer thin films can be obtained by measuring their properties while the temperature is being increased [83].

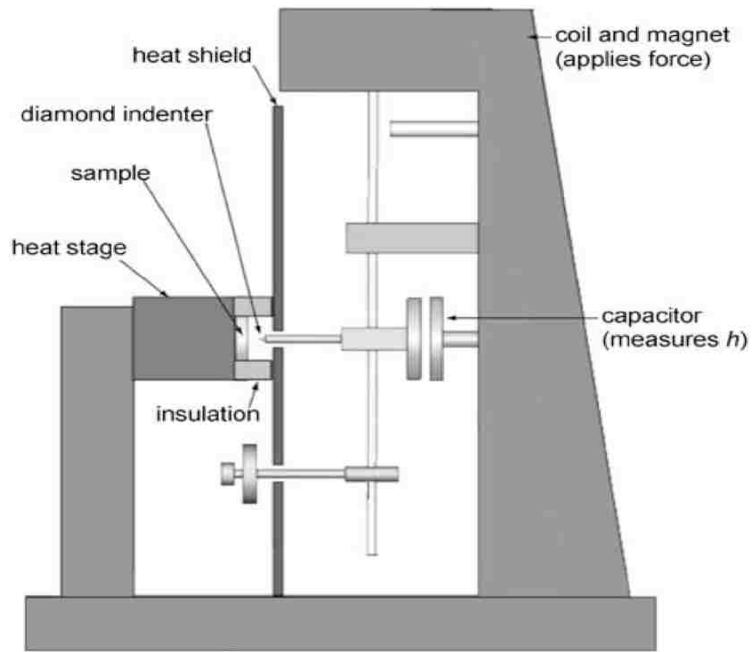


**Figure 3-13:** Schematic of the NanoTest with the hot stage (HS) installed [3]

As shown in Figure 3-13, an aluminum shield is installed in front of the pendulum. The indenter and its heater are passed through this thermal shield. The aluminum shield is utilized to prevent any thermal interference with the ambient electronics and depth sensing equipment. The sample is mounted on a ceramic thermal insulator. The sample heater is located on a thermal insulator.

To eliminate any temperature gradient in the sample and to make sure the stage and sample temperatures are the same, 3 millimeters thin samples were prepared for the hot stage.

All the displacements are highly sensitive to thermal expansion [78, 79]. The air convection due to excessive temperature of the testing area causes some noise in the depth measurements. Four strips of glass fiber insulation can be placed between the stage and shield to stop any airflow around the sample. Complete setup revealing the functionality of the hot stage is shown in Figure 3-14.

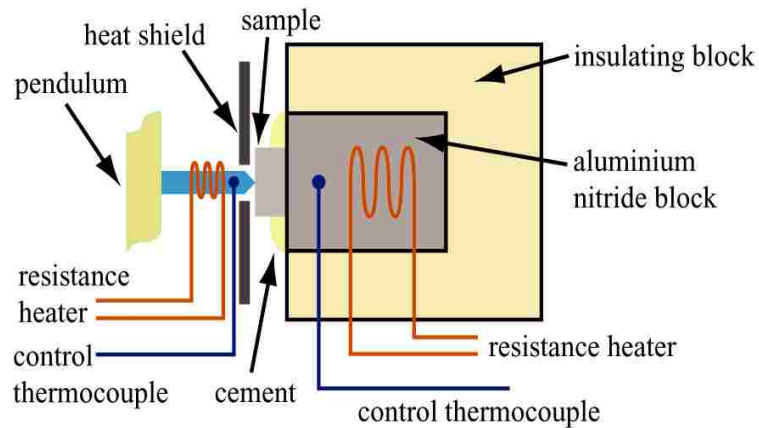


**Figure 3-14:** The set up for the Hot Stage

It is desired to measure the compliance of the machine at each temperature as the increase in the temperature gives a raise to the total compliance [57]. As long as we are doing our experiments at low loads, max 5mN, and temperatures, max 70°C, we neglect the effect of temperature on the frame compliance. Frame compliance was measured at cabinet temperature and applied to all measurements.

If necessary, frame compliance can be measured with doing 5, 200mN indents into the fused silica. Assuming that our indenter is an ideal Berkovich tip at depths correspondent to 200 mN and having the properties of fused silica we can calculate the frame compliance. A small piece of fused silica is cemented to the sample plate in



addition to the sample under the test to avoid the need for removing the stage to swap samples.

Recently, the use of a dimensionless creep parameter,  $A/d_0$ , has been investigated [82, 84], as a measure of time-dependent deformation during indentation at constant force.

$$d/d_0 = [A/d(0)] * \ln(Bt + 1) \quad (3.8)$$

where  $A$  and  $B$  are constants and  $A/d_0$  is the initial deformation at the beginning of the hold period in an indentation test and  $d$  is the increase in depth during the hold period so that  $d/d_0$  is the fractional increase in depth during creep duration. It has been shown elsewhere that values of  $A/d_0$  for a range of polymer systems appeared to correlate with  $\tan \delta$  and with the distance from the test temperature to the glass transition temperature [82].

This model can be used for the first 20-60 seconds of the creep test. Another alternative is to perform the creep test over a long period of time. The time dependent properties are not of interest of this chapter and will be discussed later in Chapter 4.

Examining the behavior of the magnetically annealed versus the neat epoxy at elevated temperatures below the glass transition temperature is of great interest. The texture in the magnetically annealed epoxy might be affected by the elevated temperature and thus it will affect the mechanical properties.

For the effect of the thermal curing of the sample on the mechanical properties, we limited the investigation to the preferred orientation; the lateral direction of the sample. Two samples were tested separately under a maximum load of 1 mN, with loading rate of 0.05 mN/s and unloading rate of 0.1 mN/s. The indentation tests were carried out at 50°C and 70°C, respectively. The glass transition temperature of the Aeropoxy is 91°C. The tests were repeated 4 times under each temperature allowing the samples to cure for 15 minutes in between each two tests before testing them again. It is apparent from Figure 3-15 and 3-16 that the modulus and hardness properties of the samples are much less than those measured under room temperature. However, the samples in general continue to cure and their hardness and modulus improve if they are allowed more time at high temperature below the glass transition of the epoxy; 91 °C.

However, the curing under high temperature, as usually predicted for thermosets, embrittled the samples evident by the reduction in the elastic and plastic work, shown in Figure 3-17. Interestingly, the samples annealed under the magnetic field, when tested along their preferred orientation (LD) direction, they showed relatively higher modulus and hardness compared to the neat epoxy samples. More tests were performed to make sure that the trend of having improved properties is valid at elevated temperatures. We are not interested in showing exact numbers for improvements but rather we have presented the plotted result as a proof to the fact that the polymer chains maintain their texture at elevated temperatures.

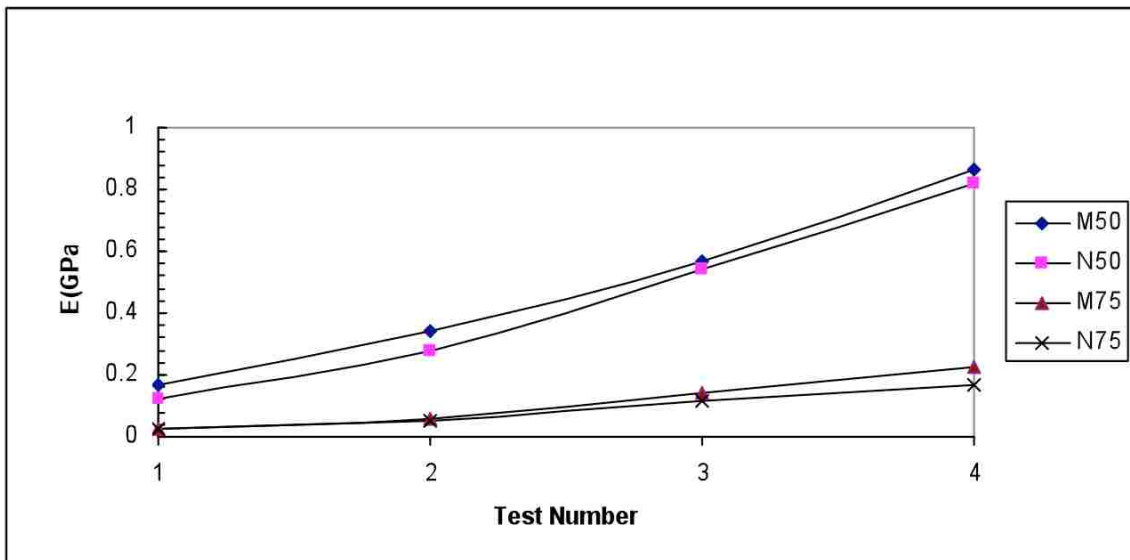


**Figure 3-15:** Reduced elastic modulus for magnetically annealed, M, and neat sample, N, at elevated temperatures of 50°C and 70°C. The sample cures as the test is progressing. The horizontal axis corresponds to time or test number. Duration between each two tests is 15 minutes.

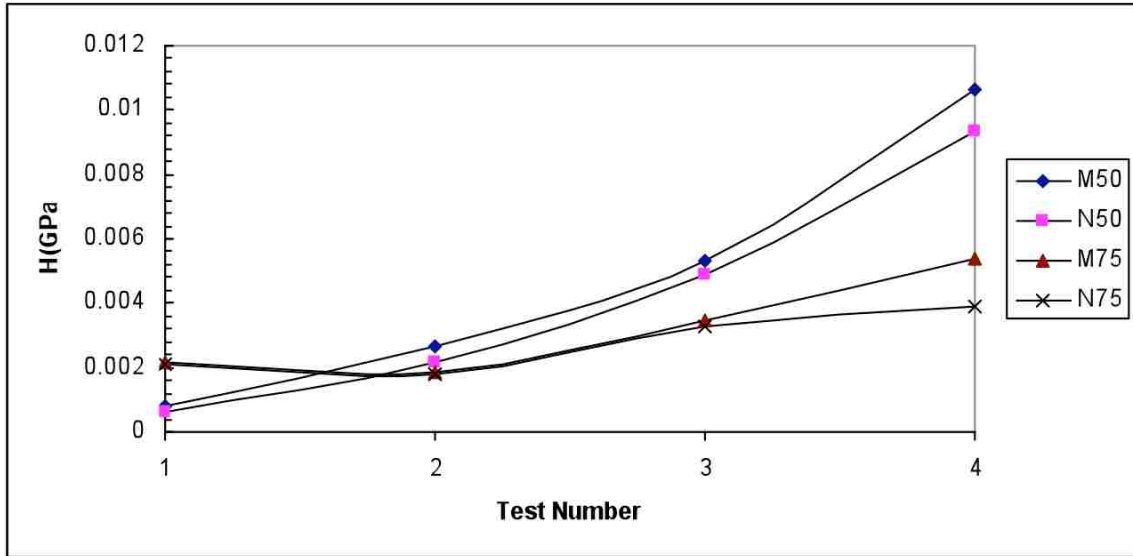


**Figure 3-16:** Hardness for magnetically annealed, M, and neat sample, N, at elevated temperatures of 50°C and 70°C. The sample cures as the test is progressing. The horizontal axis corresponds to time or test number. Duration between each two tests is 15 minutes.

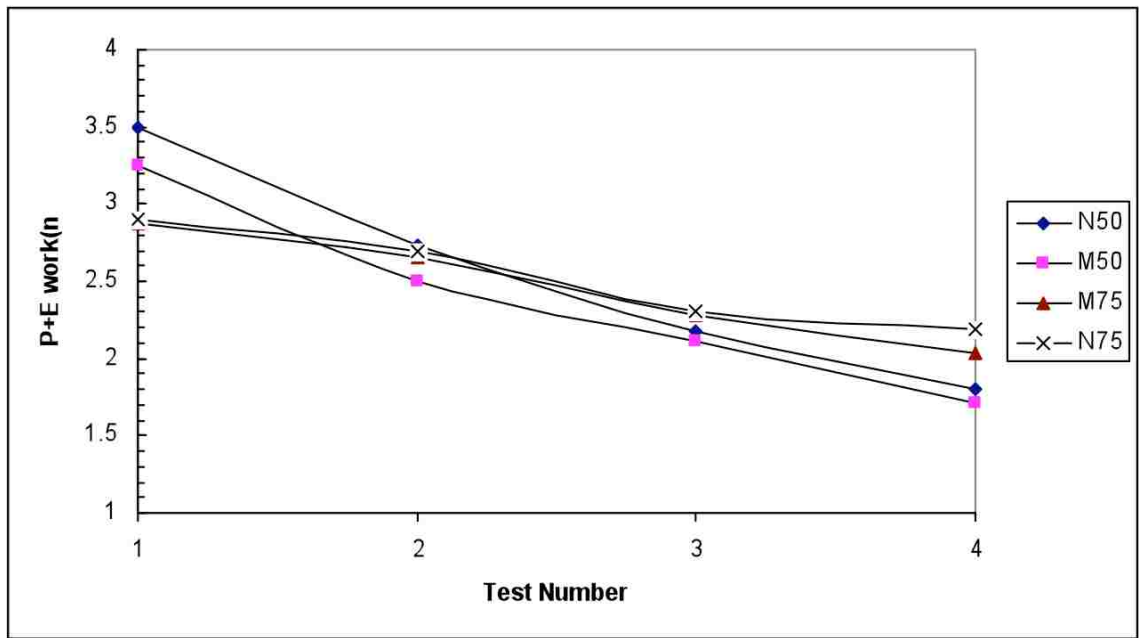


**Figure 3-17:** Plastic and Elastic work magnetically annealed, M, and neat sample, N, at elevated temperatures of 50°C and 70°C. The sample cures as the test is progressing. The horizontal axis corresponds to time or test number. Duration between each two tests is 15 minutes.

## CHAPTER 4: EFFECT OF MAGNETIC ANNEALING ON TIME – DEPENDENT BEHAVIOR

### 4.1 Nanocreep Test

Although polymeric materials show average to good mechanical properties, they possess weak creep properties. Creep is identified as the change in the length of a specimen under a constant load/stress. Creep can occur under indentation loading and manifests itself as a change of depth while the load is kept constant. Elastic and viscoelastic properties can be achieved from creep curves [68]. Analogous to macroscale test, creep can be obtained by performing the nanocreep tests over long periods of time. There are two distinguishable parts in any nanocreep curve. The first part is a sharp rise in depth as shown in Figure 4-1, which is dominant at the first few minutes of the creep test. The slope of the creep displacement-time curve remains almost constant after the first sharp stage of creep [66, 85]; secondary steady state creep.

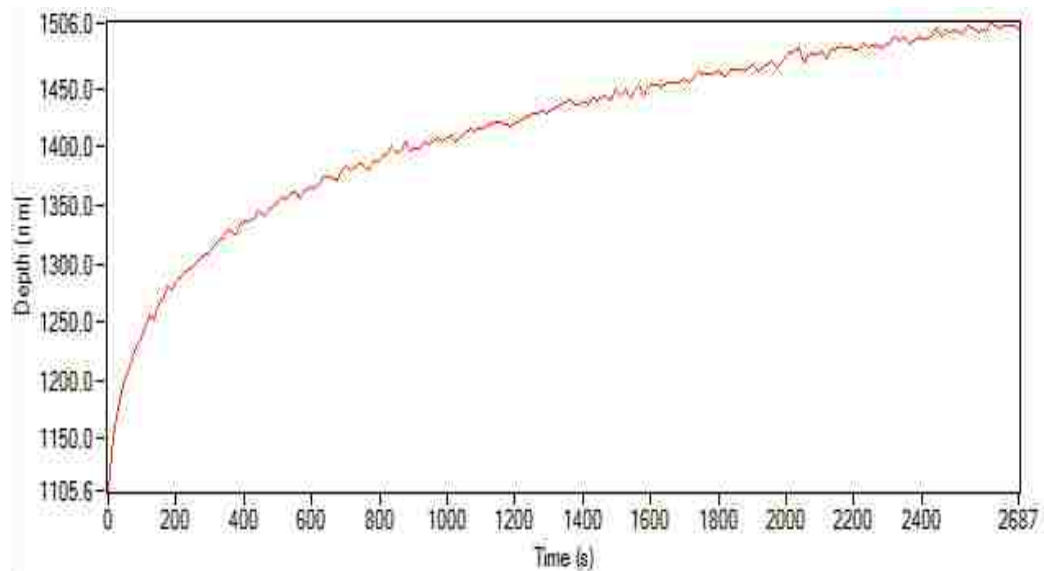


**Figure 4-1:** Depth vs. time nanoindentation creep curve for the polymer sample, maximum load 5 mN and loading rate of 0.5 mN/s were applied.

Creep tests have been carried out under the same loading condition as normal indentations (loading rate of 0.5mN/s) and the samples have been allowed to creep out for 45 min under a maximum load of 1 mN. During creep tests temperature was maintained at 25 °C using the PID-controlled thermal chamber. Two more creep testes were carried out under 1 mN maximum load and at two different temperatures of 50 °C and 75 °C, respectively.

The results of nanoscale creep tests, shown in Figure 4-2, suggest that at room temperature the magnetically annealed samples exhibit less creep deformations compared to the neat samples. This observation was repeatable in both axial and lateral directions of the samples due to the two-dimensional stretching effect of the main chains and the crosslinks of the epoxy as a result of the magnetic processing. Like the modulus and hardness, the creep resistance of the material was higher along the magnetic field direction. The improvements of the creep resistance signifies that the chain segments, *locally* reoriented normal to the sample axis, can be easily stretched along that direction compared to the orientation of the magnetic field; along the sample axis. However, at room temperature the magnetically annealed samples show more creep resistance compared to the neat samples in both MD and LD directions.

To examine if the improvement on creep resistant will be maintained at elevated temperatures, we performed separate creep tests along the lateral direction, at 50 °C and 70 °C, under the same loading conditions used at room temperature, as shown in Figure 4-3. The epoxy samples showed significant creep at these temperatures compared to room temperature; by an order of magnitude in the case of 50°C and two orders of magnitude at 70 °C. However, the samples annealed with the magnet; oriented in the LD directions, showed more creep resistance compared to the neat epoxy samples regardless of the creep thermal conditions.

At 70 °C the sample kept creeping at higher rate as the epoxy is close to the glassy state. The interdistance between chains is large and hence it is much easier to flow under constant load.

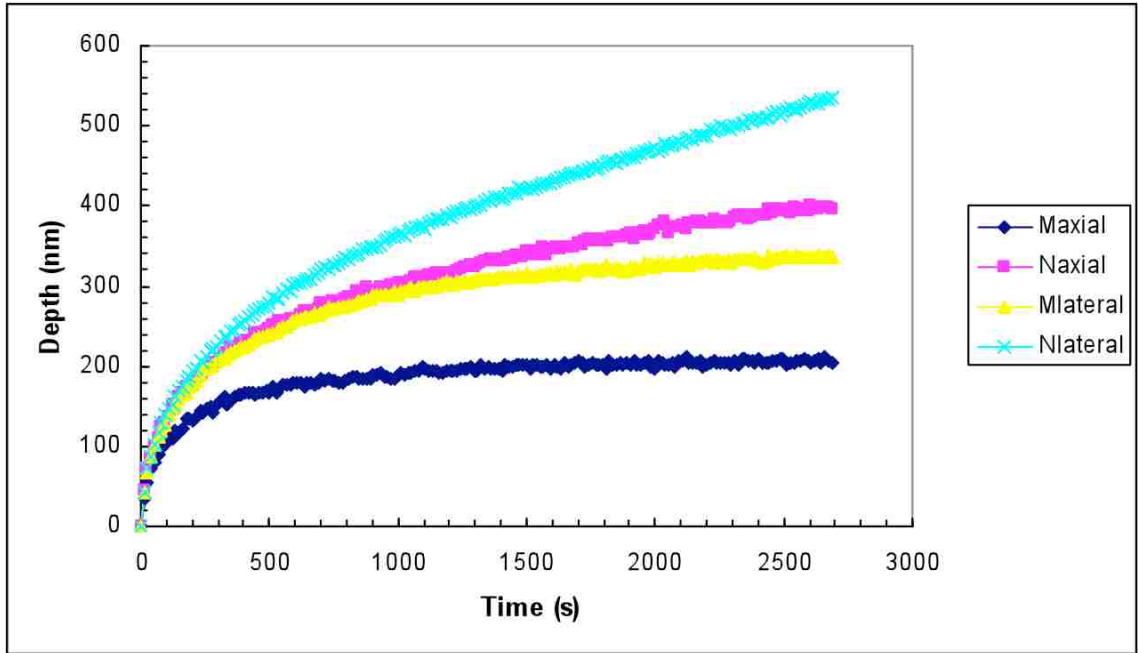


**Figure 4-2:** Nanocreep tests of epoxy samples at ambient temperature. A maximum load of 1 mN was held constant for 2700 s during the test. M and N correspond to magnetically annealed and neat sample, respectively.

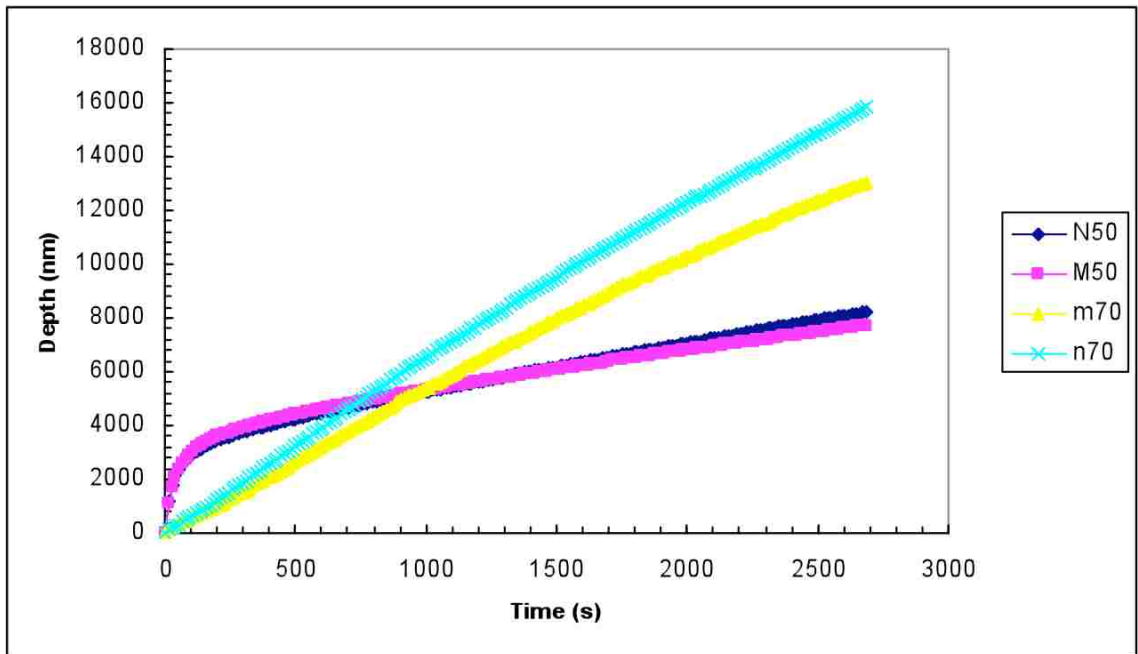


**Figure 4-3:** Nanocreep tests of epoxy samples in lateral direction at elevated temperatures of 50 and 70 °C. A maximum load of 1 mN was held constant for 2700 s during the test. M and N correspond to magnetically annealed and neat sample respectively.

## 4.2 Continuous Compliance Calculations

Typical analysis of nanoindentation rely on the fact that the displacements recovered during unloading are largely elastic, in which case the elastic punch theory can be used to determine the modulus from the unloading part of the load-depth data [60, 86, 87]. However, for polymers, the unloading behavior of polymeric materials is both elastic and viscoelastic. Hence, utilizing standard nanoindentation procedures for polymers leads to an overestimation of the elastic modulus [87-89]. Although some correction procedures have been suggested to obtain a better estimate, the elastic modulus alone does not provide a complete representation of the time dependent properties of polymers. Nanoindentation analogies of creep, stress relaxation and dynamic mechanical analysis (DMA) have been actively pursued and applied to determine the viscoelastic properties at the micro and nano length scales [86-92].

Dynamic nanoindentation or continuous contact compliance calculation (CCC), which is analogous to DMA, has received a lot of attention from researchers in the past few years [93]. In theory, the properties that can be obtained are frequency and temperature dependent and include: the storage and loss moduli, the loss tangent ( $\tan \delta$ ), the glass transition temperature,  $T_g$ , the mechanical relaxation, and the activation energy for the relaxation process. The NanoTest 600 system at UNM is not capable of doing all the above tests.

With dynamic nanoindentation, results can be obtained faster and over a wide range of frequencies and the variation of properties can also be obtained as a function of depth. Moreover, the loss tangent, which can also be obtained using this technique, has been considered by many as a measure of the viscoelasticity of a material. It does not only provide an estimate of damping and viscous energy dissipated in a material, but gives valuable information about the transition temperatures and the associated activation energies when it is used along with the hot-stage. CCC can be very useful in characterizing the viscoelastic properties of polymers, polymer coatings and surface modified polymers. It can also be used to determine the variation of viscoelastic properties in heterogeneous materials like polymer composites and biological tissues.

Finally, in addition to determining the viscoelastic properties, dynamic indentation can also find application in the characterization of dynamic contacts in MEMS and in contact processes like dry friction, abrasive and erosive wear [88, 90, 91].

The results from these methods are comparable to the DMA data for the bulk material and show a good agreement [88]. CCC uses an oscillating sample and measures the phase difference between the input sample oscillations and the depth output of the indenter probe. This method eliminates a lot of uncertainties we have in regular analysis of nanoindentation curve and enables us to record the properties as a function of depth, which is really useful in case of amorphous thin films and materials.

The first derivative of the indentation load,  $p$ , with respect to the indentation depth,  $h$ , is related to the material properties via,

$$\frac{dp}{dh} = 2\sqrt{\frac{A}{\pi}} \frac{E}{1-\nu^2} \quad (4.1)$$

Where  $E$  and  $\nu$  are the reduced modulus and Poisson's ratio of the material respectively. The elastic parameters can be replaced by viscoelastic ones. Hence,

$$\frac{dp^*}{dh} = 2\sqrt{\frac{A}{\pi}} \frac{E^*}{1-\nu^2} \quad (4.2)$$

For a hold period the load and the depth can be written as,

$$\Delta P = P_0 e^{i(\omega t + \delta)} \quad (4.3.a)$$

$$\Delta h = h_0 e^{i(\omega t)} \quad (4.3.b)$$

Where  $\omega$  and  $\delta$  are the frequency of the oscillations and phase shift between the input load and output depth, respectively. Substituting (4.3.a) and (4.3.b) into (4.2) results in,



$$E_r^* = \frac{1}{2} \sqrt{\frac{\pi}{A}} (S + iC\omega) \quad (4.4)$$

Where S and C are the dynamic contact stiffness and dynamic contact damping, respectively. For CCC analysis the Nanoindenter can be simply modeled as shown in Figure 4-4.

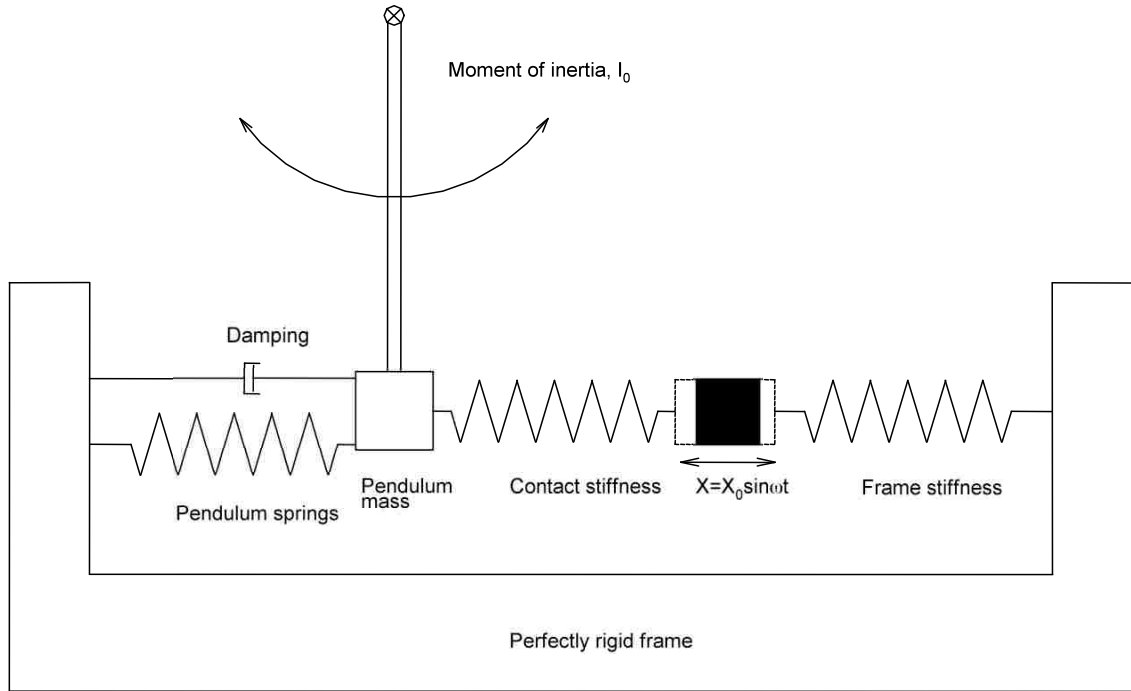


**Figure 4-4:** Spring dashpot model for the continuous contact compliance measurement.

A viscoelastic spring–dashpot model of the material-indenter setup with contact stiffness,  $k'$ , and a contact damping,  $c'$ , in parallel, was assumed. The schematic of the setup with the sample in place is shown in Figure 4.5. The governing equation of the system is given by:

$$m \frac{d^2 y}{dt^2} + (c' + c_0) \frac{dy}{dt} + (k' + k_0) y = c' \frac{dx}{dt} + k' x \quad (4.5)$$

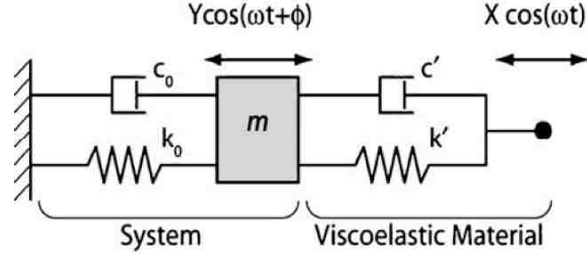


**Figure 4-5:** Spring dashpot model of the test setup with the sample in place [88].

This second order ODE can be solved to get the phase difference between oscillations of the sample and the indenter:

$$\phi = \arctan \left[ \frac{\omega(c_0 + c')}{k_0 + k' - m\omega^2} \right] + \arctan \left( \frac{c'\omega}{k'} \right) + \phi_0 \quad (4.6)$$

The term  $\phi_0$  is the electronics (static error) contribution to the phase offset. Continuous compliance measurements have been carried out at depths over one micron to make sure that the tip can be assumed an ideal Berkovich tip. This will lead to a contact stiffness proportional to the contact depth. The contact damping is also assumed to be proportional to the depth [88]. This assumption leads to a loss modulus value that is independent of the depth. Thus equation (4.6) can be rewritten as,

$$\phi = \arctan \left[ \frac{\omega(c_0 + cx)}{k_0 + kx - m\omega^2} \right] + \arctan \left( \frac{c\omega}{k} \right) + \phi_0 \quad (4.7)$$

where  $x$  is the contact depth and  $c$  and  $k$  are constants.

The parameters in equation (4.7) can be calculated with the use of a rigid pin and a spring as explained below.

A rigid pin of about the same diameter of the indenter holder hole was used to attach the sample stage to the indenter holder. This rigid connection with the damping plates removed is used to calculate the frame compliance and the phase contribution of the electronics. This rigid pin will eliminate any stiffness or damping effect except for the

machine ones. All of the calibrations were performed at the same frequency and position of the pendulum as for the actual testing.

A frame compliance of 0.51 nm/mN was calculated using the data obtained from ramping up and unloading the load with the indenter and the stage soldered together. A peak load of 500 mN and a rate of 50 mN/sec were used. The load was slowly ramped up to 10 mN and held for 80 seconds. Phase shift measurement was collected during the hold period. This test was done at the same frequency of 10Hz as the actual test. The parameter  $c_0$ , Figure 4-6, is approximately zero when the damping plates are removed. The only phase shift is due to the electronics.

A spring with the stiffness of 2908 N/m was used to attach the sample stage to the indenter holder. The spring stiffness was found from the data obtained from loading and unloading the spring up to 200 mN with a rate of 25 mN/s.

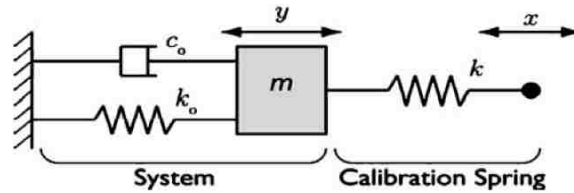


**Figure 4-6:** Spring dashpot model with the calibration spring in place [88].

The pendulum resonant frequency was found using the measurements made on a wide range of frequencies while measuring the displacement of the pendulum. The maximum displacement corresponds to the resonant frequency of the pendulum. Resonant frequency of the pendulum found to be 16.9 Hz.

Knowing the spring stiffness and the resonant frequency of the pendulum we can calculate the pendulum effective mass,

$$2\pi f_1 = \omega_1 = \sqrt{\frac{s}{m}} \quad (4.8)$$

Where  $f_1$  = frequency,  $\omega_1$  = angular frequency,  $s$  = spring stiffness, and  $m$  = effective mass of the pendulum.

Both the instrument frame stiffness and the pendulum support spring stiffness are ignored.  $f_1$  is actually the frequency for velocity resonance, i.e. the frequency at which maximum velocity occurs. The amplitude resonance frequency which the machine measures is given by:

$$2\pi f_2 = \omega_2 = \sqrt{\left(\frac{s}{m} - \frac{C^2}{2m^2}\right)} \quad (4.9)$$

In practice,  $f_1$  and  $f_2$  are very close. An effective mass of 0.2579 kg was calculated using equation (4.8).

After collection of phase data with a known spring installed and carrying out the calibrations, the system damping is found by rearranging equation (4.7):

$$C = \left(\frac{k + K - m\omega^2}{\omega}\right) \tan(\varphi - g) \quad (4.10)$$

This calibration should be done at a frequency which will not be influenced by resonance effects. The results are dependent on the damping plate spacing, so this distance must remain constant after calibration.

It has been found that eddy current damping can also contribute to the system damping, especially at higher frequencies [58]. It may be necessary, therefore, to produce a curve of system damping vs. frequency if a range of frequencies is to be investigated. For our work all the tests were done at 10 Hz. The measured system damping over depths of 1-4 microns was 10 N.s/m.

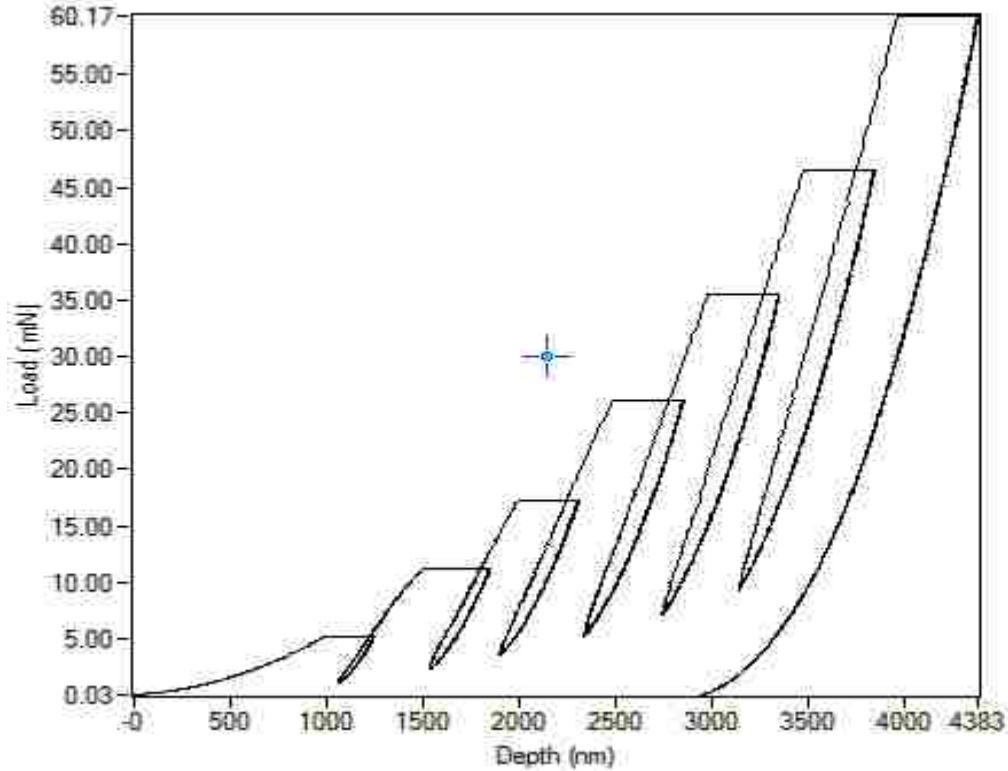


**Figure 4-7:** Cyclic load-hold-partial unload indentations on epoxy for measuring phase during hold period

As shown in Figure 4-7, a set of loading -partial unloading indentations was produced, with the phase angle being measured during the dwell period. A loading rate of 0.5 mN/s and unloading rate of 0.1 mN/s were used. CCC data collected over seven 80 seconds dwell periods over the depth range of 1-4 microns. The second halves of the CCC data were averaged out. Some time is required for the machine to stabilize after each loading. The first half of the dwell time was considered for this task. These data are used for the measurement of the complex modulus. The contact depth is usually found from the unloading curve using the Oliver–Pharr analysis [94] assuming elastic deformation. But this procedure is known to give erroneous results for viscoelastic materials. Alternative procedures for calculating the contact depth for viscoelastic contacts from the initial section of the unloading curve have been suggested by Tang et al.[95]. But for the purpose of this study on epoxy, because the sample piles up as the indenter penetrates through, the actual depth of penetration of the indenter into the material provides a better approximation for the contact depth. Some proposed models

are available to compensate for the overestimation in mechanical properties due to the pile up. This assumption is supported by the AFM imaging of an indentation on the material as shown in Figure 4-8.

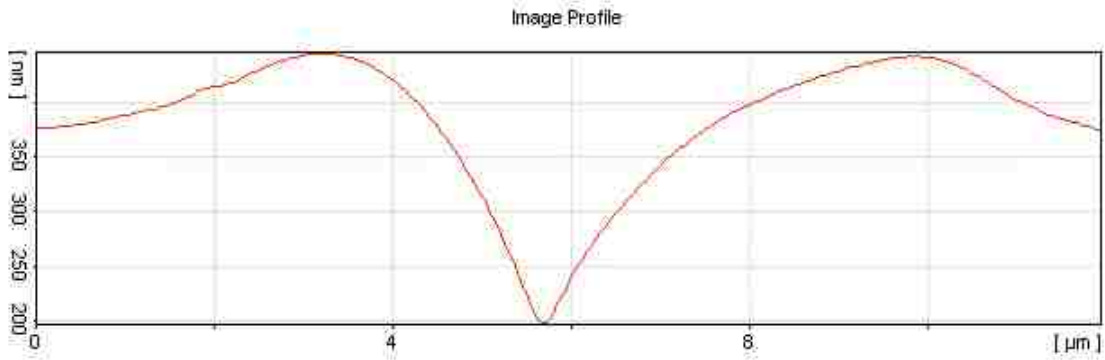


**Figure 4-8:** Cross section of a nanoindentation showing pile up

Since all parameters of equation (4.7) are known, a curve fit of the phase versus depth will allow us to determine the contact compliance and damping. Figure 4-9 shows the CCA data and the model curve fit to it for the neat sample.

The storage  $E'$  and loss moduli  $E''$  can be calculated using,

$$E' = \frac{k}{2} \sqrt{\frac{\pi}{24.5}} \quad (4.11)$$

$$E'' = \frac{c\omega}{2} \sqrt{\frac{\pi}{24.5}} \quad (4.12)$$

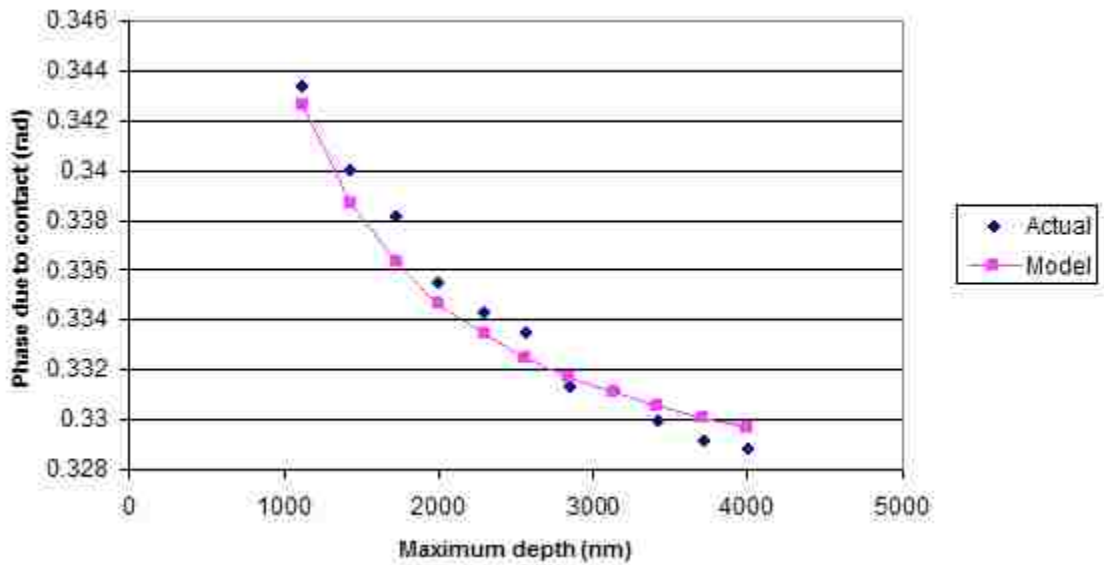


**Figure 4-9:** A representative of the model fit to the experimental phase shift versus depth curve of the polymer sample

The viscoelastic properties were measured in the lateral direction for both neat and magnetically annealed samples are shown in Table 4-1. The magnetically annealed sample shows less viscoelastic behavior in the LD direction, evident by the lower  $\tan \delta$ . The results from the CCC analysis verifies the results from the 45 minutes creep tests in section 4-1, and shows better creep properties for the magnetically annealed samples.

**Table 4-1** Viscoelastic properties measured in the ND direction on the lateral side of the samples

	Storage Modulus (GPa)	Loss Modulus (GPa)	$\tan \delta$
Magnetically annealed	4.84	0.0316	0.00653
Neat	4.63	0.0335	0.00724
Percentage Change%	4.5	-5.7	-9.8

## CHAPTER 5 CONCLUSIONS AND FUTURE WORK

### 5.1 Conclusions

Diamagnetic materials align parallel to the high magnetic fields where the levitation or micro gravity effect causes the chains to overcome their weight and align in the field direction [18, 28, 5]. Magnetic fields which are still high but not large enough to produce levitation can align the diamagnetic molecules and chains diamagnetically in a plane perpendicular to the field as shown in the studies done by Kimura et al. and Douglas et al. [23-25, 29, 33, 34, 41, 96]. The orientation schematic is shown below in Figure 5-1. Diamagnetism based alignment can even occur at magnetic fields as low as 0.5 Tesla. This has been shown in the investigations done by Gerzeski [42, 45].

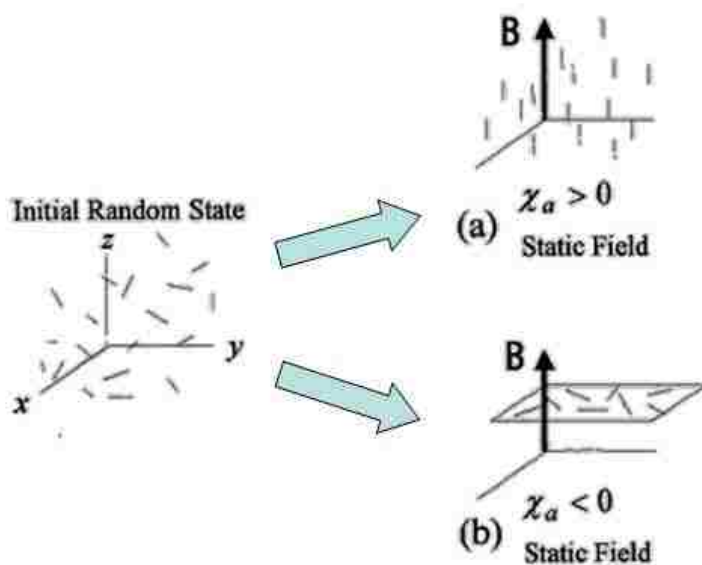


**Figure 5-1:** Alignment of an anisotropic particle with (a) levitation effect and (b) diamagnetism effect under a static field [23].

WAXD is a very useful technique to examine the amorphous orientations in polymeric materials. For the case of this study it provided a plethora of information regarding the orientations of the aligned chains in the samples. The depth of the X-ray



beam which was used in our study, into the material surface was about 200 microns. This has given us information not only for shallow depths and the surface but for a thin 200 microns layer of the polymer. The 2 theta scans verified the existence of a texture evident by the halo at  $19^\circ$ . The diamagnetic effect due to the field will result in a texture in both ND and LD directions in a bi-axial fashion. All the pre-orientations in the lateral direction of neat sample, evident by the peaks in Figure 2-9, upon applying the magnetic field have been suppressed to one peak, Figure 2-10, around  $90^\circ$  which corresponds to the LD direction.

Based on the pole figure generated, there was some initial orientation in the neat samples confirmed with the texture results. This initial orientation can be attributed to: (1) gravity, (2) wall effect and (3) Degassing. Gravity will induce an orientation in the MD direction. Curing of the samples starts from the walls of the sample and proceeds to the inner core of the material. This will result in a texture induced by the walls of the containers. Furthermore, the samples were curing while they were being degassed under vacuum. Gas bubbles are likely to induce a texture as they are moving upward in the MD direction. All of the above effects are present in the MD direction of the sample while the only one present in the ND direction is the wall effect.

Pole figures generated from phi scans are very beneficial in the manner that they show quantitatively, the 3D texture in a 2D fashion and contain all the information in a spatial space. The Phi scan of the neat sample and magnetically annealed ones showed the disappearance of some of the preorientations (peaks) and the emerging of new orientations upon applying the magnetic field. The evolution of these orientations was captured quantitatively by the pole figures. The pole figure analysis used for this study reveals the creation of textures biaxially, due to the magnet effect, in planes that are not aligned with the magnetic field. The pole figure also revealed the significant texture due to gravity that was observed even after the magnetic annealing. Therefore from the pole figure one can conclude that while the magnetic annealing induced new texture, the texture generated due to gravity and wall effect was dominant in the samples.

Probing the mechanical properties of the epoxy upon magnetic annealing can provide an indirect quantitative measure of the enhancement on the microstructure and thus the mechanical performance of the epoxy system. While macroscale mechanical testing can provide a full range of information, but such a testing scale will require a large scale sample and the measured properties will be averaged (homogenized) over dimensions not necessarily affected by the magnetic field; the magnetic field effect might not be noticed. On the other hand, for the case of thin films where the magnetic field effect prevails just in shallow depths of the material, nanoindentation should be employed to examine the mechanical properties.

Nanoindentation techniques were not present in the 70's and early 80's at the time when low magnetic fields were employed to improve polymer's properties with use of low magnetic fields. Using nanoindentation, improvements in both axial and lateral directions of the sample has been observed. The Young's modulus and hardness in the lateral direction (LD) under loads of 5 mN have been both improved by 6.6%. The polymer chains owing to their diamagnetic nature get densified in the ND and LD directions due to the biaxial reorientation and that explains the improvements on the hardness and Modulus along these directions. However, the plastic plus elastic work has decreased by 4.3% under the same load indicating that the magnetic field embrittled the epoxy. Using high loads (5mN) in the MD direction revealed that no improvement in deeper depths is achieved as the magnetic field effect fades away at larger depths (loads).

Hot stage nanoindentation is a useful technique to obtain the properties in the operating temperatures that the material might be exposed to. For the case of this study the samples were still curing while the hot stage tests were utilized. Therefore, a range of the properties is achieved over different thermal environments. In-situ curing of the magnetically annealed samples during the nanoindentation showed better mechanical properties at elevated temperatures compared to the neat samples. The goal was to show that the texture which has been induced upon magnetic field application can be maintained at elevated temperatures.

The analysis of the time dependent behaviour of polymers is of great importance to quantify their long-term performance. Creep tests over 45 minutes analogous to macro creep, has shown a constant slope in depth vs. time curve beyond the first few minutes of the creep test; steady state creep. The steady state creep rate of the magnetically annealed sample in both directions was reduced in both ambient and elevated temperatures of 50 and 70°C. compared to the neat epoxy. Thus, magnetic annealing increased the creep resistance of the epoxy.

Continuous contact compliance (CCC) test analogous to the macroscale dynamic mechanical analysis (DMA) test is a very useful tool in determining the parameters by which the long-term viscoelastic behavior of polymers can be estimated. The viscoelastic properties derived from DMA analysis takes very long times to be obtained from creep and/or stress-relaxation tests at macro-scale. Similarly, CCC enables us to find the valuable loss and storage moduli and the  $\tan \delta$  in relatively short times. Based on the CCC analysis the storage modulus of the magnetically annealed epoxy was improved by 4.5 % while its loss modulus decreased by 5.7%. These changes in the moduli were accompanied by an improvements in  $\tan \delta$  by 9.8% for the magnetically annealed samples over the neat epoxy samples.

Overall, using permanent magnets is useful in improving mechanical properties and the viscoelastic performance of the polymer thin films or just the surface of the polymers.

## 5.2 Future Work

- Moderate magnetic field can be utilized align CNTs in a polymeric medium, if we add paramagnetic or ferromagnetic nanoparticles to the epoxy mix.
- Other orientation characterization techniques such as polarized microscopy or wide angle scattering instead of diffraction should be tried to provide further information about the magnetic induced alignment of the amorphous epoxy.

- Different epoxy systems with different viscosities range (low to high) should be tried with viscosity as a parameter to investigate the effect of magnetic annealing.
- Nanoscratch and nano-impact tests should be examined to show the changes on the other properties of the polymer due to the magnetic annealing such as wear resistance and impact behavior.
- CCC testing at higher temperatures can provide good information on the viscoelastic nature of the improved samples at higher working temperatures.

## Bibliography

1. Kawakami, D., B.S. Hsiao, C. Burger, S. Ran, C. Avila-Orta, I. Sics, T. Kikutani, K.I. Jacob, B. Chu. Deformation-induced phase transition and superstructure formation in poly(ethylene terephthalate), *Macromolecules*, 2005, 38: 91-103.
2. Kocks, U.F., V.N. Tome, H.R. Wenk. *Texture and Anisotropy*. 1998, New York, NY: Cambridge University Press.
3. Juliano, T.F., M.R. VanLandingham, C.A. Tweedie and K.J. Van Vliet. Multiscale Creep Compliance of Epoxy Networks at Elevated Temperatures, *Experimental Mechanics*, 2007, 47: 99-105.
4. Al-Haik, M.S., H. Garmestani, A. Savran. Explicit and Implicit Viscoplastic Models for Polymeric Composite, *International Journal of Plasticity*, 2004, 20 : 1875-1907.
5. Garmestani, H., M.S. Al-Haik, K. Dahmen, R. Tannenbaum, D.S. Li, S.S. Sablin, M.Y. Hussaini. Epoxy Mediated Alignment of Single Wall Carbon Nanotubes Under High Magnetic Fields, *Advanced Materials*, 2003, 15: 1918-1922.
6. Shiota, A. and C.K. Ober. Orientation of Liquid Crystalline Epoxides under ac Electric Fields. *Macromolecules*, 1997, 30: 4278-4287.
7. Su, W.F. K.C. Chen, and S.Y. Tseng. Effects of Chemical Structure Changes on Thermal, Mechanical and Crystalline Properties of Rigid Rod Epoxy Resins. *Journal of Applied Polymer Science*, 2000, 78: 446-451.
8. Scherzer, T. Molecular Orientation in Novolac Cured Epoxy Resins as Studied by Rheo-optical FTIR Spectroscopy. *Journal of Applied Polymer Science*, 1998, 70: 247-259.
9. Muthukumar, M., C.K. Ober, E.L. Thomas. Competing Interactions and Levels of Ordering in Self-Organizing Polymeric Materials. *Science*, 1997, 277: 1225-1232.
10. Christianen, P.C., I.O. Shklyarevskiy, M.I. Boamfa, J.C. Maan. Alignment of molecular materials in high magnetic fields. *Physica B*, 2004, 346-347: 255-261.
11. Geiger, K., K. Knoll, and M. Langela. Microstructure and rheological properties of triblock copolymers under extrusion conditions. *Rheol Acta*, 2002, 41: 345-355.
12. Son, Y., K.H. Ahn, and K. Char. Morphology of Injection Molded Modified Poly(phenylene oxide)/Polyamide-6 Blends. *Polymer Engineering and Science*, 2000, 40: 1376-1381.

13. Kabeel, M.A. Interferometric determination of (skin–core) optical and orientation structural parameters of drawn polypropylene fibres. *Journal of Physics: Condensed matter*, 2001, 13: 353-364.
14. Kudaibergenov, S.E., V.B. Sigitov, A.G. Didukh, E.A. Bekturov, I.E. Suleimenov. Behavior of Polyelectrolyte Gels under the Influence of d.c. Electric and Magnetic Fields. *Polymer for Advanced Technologies*, 2000, 11: 805-809.
15. Holstein, P., M. Bender, M. Winkler, D. Geschke. Reorientation of a Liquid Crystalline Side-chain Polymer in Electric and Magnetic Fields Investigated by Solid-state H-NMR. *Polymers for Advanced Technologies*, 1998, 9: 659-664.
16. Suleimenov, I.E., V.B. Sigitov, S.E. Kudaibergenov, A.G. Didukh, T.S. Fryasinova, E.A. Bekturov. Influence of combined magnetic and electric fields on the behaviour of polyelectrolyte hydrogel. *Polymer International*, 2001, 50: 194-196.
17. Martin, D.C. Controlled local organization of lyotropic liquid crystalline polymer thin films with electric fields. *Polymer*, 2002, 43: 4421-4436.
18. Al-Haik, M.S., H. Garmestani, D.S. Li, M.Y. Hussaini, S.S. Sablin, R. Tannenbaum, K.H. Dahmen. Mechanical Properties of Magnetically Oriented Epoxy. *Journal of Polymer Science Part B: Polymer Physics*, 2004, 42: 1586-1600.
19. Assender, H.E. and A.H. Windle. Domain structures in magnetically oriented liquid crystalline polymers. *Polymer*, 1997, 38(3): p. 677-688.
20. Benicewicz, B.C., M.E. Smith, J.D. Earls, R.D. Priester Jr, S.M. Setz, R.S. Duran, E.P. Douglas. Magnetic Field Orientation of Liquid Crystalline Epoxy Thermosets. *Macromolecules* 1998, 31: 4730-4738.
21. Gerzeski, R. Attempts to Enhance the Properties of EPON 830=4,4'-Methylene Bis Cyclohexylamine Epoxy Resin Systems by Exposing Them to 0.1290 to 0.8810 Tesla. *Polymer Engineering and Science*, 1999, 39:2150-2158.
22. Holstein, P., M. Bender, M. Winkler, D. Geschke. Reorientation of a Liquid Crystalline Side-chain Polymer in Electric and Magnetic Fields Investigated by Solid-state H-NMR. *Polymers for Advanced Technologies*, 1998, 9: 659-664.
23. Kimura, T.. Study on the Effect of Magnetic Fields on Polymeric Materials and Its Application. *Polymer Journal*, 2003, 35: 823-843.
24. Kossikhina, S.A., T. Kimura, E. Ito, M. Kawahara. Thermomechanical Properties of a Magnetically and Mechanically Oriented Liquid Crystalline Copolyester Xydar. *Polymer Engineering and Science*, 1998, 38: 914-921.

25. Lincoln, D.M. and E.P. Douglas. Control of Orientation in Liquid Crystalline Epoxies via Magnetic Field Processing, *Polymer Engineering and Science*, 1999, 39: 1903-1912.
26. Tan, C., H. Sun, B.M. Fung, B.P. Grady. Properties of Liquid Crystal Epoxy Thermosets Cured in a Magnetic Field. *Macromolecules*, 2000, 33: 6249-6254.
27. Yamagishi, A., T. Takeuchi, T. Higashi, M. Date. Diamagnetic Orientation of Polymerized Molecules under High Magnetic Fields. *Journal of Physical Society of Japan*, 1989, 58: 2280-2283.
28. Camponeschi, E., R. Vance, M. Al-Haik, H. Garmestani, R. Tannenbaum. Properties of Carbon Nanotube-Polymer Composites Aligned in a Magnetic Field. *Carbon*, 2007, 45: 2037-2046.
29. Aoki, H., M. Yamato, and T. Kimura. Magnetic Alignment of Poly(carbonate). *Chemistry Letters*, 2001: 1140-1141.
30. Chiriac, A.P. Polymerization in a Magnetic Field. 14. Possibilities to Improve Field Effect during methyl acrylate Polymerization. *Journal of Applied Polymer Science*, 2004, 92: 1031-1036.
31. Maret, G., K. Dransfeld. Mesogene-Polymer Backbone Coupling in Side-Chain Polymer Liquid Crystals, Studied by High Magnetic-Field-Induced Alignment. *Topics in Applied Physics Springer,Verlag, Berlin (1985)*, Chap. 4.
32. Kawamura, Y., I. Sakurai, A. Ikegami, and S. Iwayanagi. Magneto-Orientation of Phospholipids, *Mol. Cryst. Liq. Cryst.*, 1981, 67: 77-87.
33. Kawai, T., R. Iijima, Y. Yamamoto, T. Kimura. Crystal Orientation of N,N'-Dicyclohexyl-2,6-naphthalenedicarboxamide in High Magnetic Field, *J. Phys. Chem. B*, 2001, 105 (34): 8077-8080.
34. Kimura, T., M. Yoshino, T. Yamane, M. Yamato, and M. Tobita. Uniaxial Alignment of the Smallest Diamagnetic Susceptibility Axis Using Time-Dependent Magnetic Fields, *Langmuir*, 2004, 20 (14): 5669-5672 .
35. Timbrell, V. Alignment of carbon and other man-made fibers by magnetic fields ,*J. Appl. Phys.*, 1972, 43: 4839.
36. Schmitt, Y., C. Paulick, F.X. Royer, and J.G. Gasser. Magnetic field induced orientational order of conductive fibers in non-conductive liquids, *Non-Cryst. Solids*, 1996, 139:205-207.

37. Revol, J.F., L. Godbout, X.M. Dong, D.G. Gray, H. Chanzy, G. Maret. Chiral nematic suspensions of cellulose crystallites; phase separation and magnetic field orientation, *Liq. Cryst.*, 1994, 16: 127.
38. Sugiyama, J., H. Chanzy, G. Maret. Orientation of cellulose microcrystals by strong magnetic fields. *Macromolecules*, 1992, 25: 4232-4234.
39. Al-Haik, M.S., M.Y. Hussaini, Molecular Dynamics Simulation of Reorientation of PE Chains under a High Magnetic Field. *Molecular Simulation*, 2006, 32(8): 601-608.
40. Al-Haik, M.S., M.Y. Hussaini, Molecular Dynamics Simulation of Magnetic Field Induced Orientation of nanotube-Polymer Composite. *Japan Journal of Applied Physics*, 2006, 45(11): 8984-8987.
41. Harada, M., M. Ochi, M. Tobita, T. Kimura, T. Ishigaki, N. Shimoyama and W. Aoki. Thermomechanical Properties of Liquid-Crystalline Epoxy Networks Arranged by a Magnetic Field. *Journal of Polymer Science Part A: Polymer Chemistry*, 2004, 42(5): 758 - 765.
42. Gerzeski, R. Soviet Efforts to Enhance the properties of Epoxies used in various Applications by Simultaneously Curing the Epoxy and Exposing it to a Magnetic Field. in 19th International SAMPE Technical Conference. 1987: SAMPE.
43. Kestelmann, V.N., S.S. Negmatov, and C.V. Sadykov. Investigation of the properties of Plastic Coating Modified in a Magnetic Field. *plastic and kautschuk*, 1980, 27(8): 448-451.
44. Molchanov, Y.M., E.R. Kisis, Y.P. Rodin. Changes in the Structure of Polymeric materials in a magnetic Field. *Mekhanika Polimerov*, 1973, 4: 737-739.
45. Gerzeski, R., *Attempts to Enhance the Properties of EPON 830=4,4'-Methylene Bis Cyclohexylamine Epoxy Resin Systems by Exposing Them to 0.1290 to 0.8810 Tesla*, *Polymer Engineering and Science*, 1999. **39**: 2150-2158.
46. Assender, H.E., A.H. Windle. The relaxation of a magnetically oriented liquid crystalline polymer. *polymer*, 1996, 37: 371-375.
47. Al-Haik, M., M.R. Vaghar, H. Garmestani, M. Shahavy. Viscoplastic Analysis of Structural Polymer Composites Using Stress-Relaxation and Creep Data. 2001, 32: 165-172.
48. Peschanskaya, N.N., P.N. Yakushev. Polymer creep in a static magnetic field. *Phys. Solid State* 1997, 39: 1690-1692.



49. Al-Haik, M.S., H. Garmestani, D.S. Li, M.Y. Hussaini, S.S. Sablin, R. Tannenbaum, K.H. Dahmen. Mechanical properties of magnetically oriented epoxy. *Journal of Polymer Science Part B-Polymer Physics*, 2004, 42(9): 1586-1600.
50. Murthy, N.S., C. Bednarczyk, P.B. Rim, C.J. Nelson. Measurement of Amorphous Orientation in Poly (ethyleneterephthalate) Fibers by X-Ray Diffraction and Its Significance. *J. Appl. Polym. Sci.* 1997, 64: 1363-1371.
51. Cullity, B.D., S.R. Stock, *Elements of X-Ray Diffraction*. 2001, Upper Saddle River, NJ: Prentice-Hall.
52. Pazur, R.J., R.E. Prud'homme. X-ray Pole Figure and Small Angle Scattering Measurements on Tubular Blown Low-Density Poly(ethylene) Films. *Macromolecules*, 1996., 29(1): 119-128.
53. Huang, C.I., J-R. Chen, Crystallization and Chain Conformation of Semicrystalline and Amorphous Polymer Blends Studied by Wide-Angle and small-Angle Scattering. *Journal of Polymer Science: Part B: Polymer Physics*, 2001, 39: 2705-2715.
54. Sperling, L.H. *Introduction to Physical Polymer Science*. 2006, Hoboken, New Jersey: Wiley-Interscience.
55. Al-Haik, M.S., H. Garmestani, A. Savran. Explicit and Implicit Viscoplastic Models for Polymeric Composite. *International Journal of Plasticity* 2004, 20: 1875-1907.
56. Kallend, J.S., et al. popLA - An Integrated Software System for Texture Analysis. in *Ninth International Conference on Textures of Materials*. 1991: Gordon & Breach.
57. Beake, B., S. Goodes, S. Jones, R. Parkinson, N. Pickford and J. Smith, *NanoTest Manual Version 3.0* 2006.
58. Oliver, W.C. and G.M. Pharr. An improved technique for determining hardness and elastic modulus using load and displacement sensing indentation experiments. *J. Mater. Res.* 1992, 7: 1564-1583.
59. Feng, G., A.H. Negan. Effects of creep and thermal drift on modulus measurement using depth-sensing indentation. *J. Mater. Res.*, 2002, 17: 660 - 668.
60. VanLandingham, M.R., J.S. Villarrubia, W.F. Guthrie, G.F. Meyers. Nanoindentation of Polymers: An Overview. *Macromolecular symposia*. 2001, 167(1): 15-44.

61. Beake, B.D., S. Chen, J.B. Hull, F. Gao. Nanoindentation behavior of clay/Poly (Ethylene oxide) Nanocomposite. *Journal of Nanoscience and Nanotechnology*, 2002, 2: 73-79.
62. Fischer-Cripps, A.C. A simple phenomenological approach to nanoindentation creep *Materials Science and Engineering A*, 2004, 385(1-2): 74-82.
63. Huber, N., E. Tyulyukovskiy. A new loading history for identification of viscoplastic properties by spherical indentation. *J. Mater. Res.*, 2004, 19: 101-113.
64. Oyen, M.L. Spherical indentation creep following ramp loading. *Proceedings of Mat. Res. Soc.*, 2004.
65. Chenga, L., X. Xiab, L.E. Scrivena and W.W. Gerberich. Spherical-tip indentation of viscoelastic material *Mechanics of Materials*, 2005, 37(1): 213-226.
66. Oyen, M.L., R.F. Cook. Load-displacement behavior during sharp indentation of viscous-elastic-plastic materials. *Proceedings of Mat. Res. Soc.* 2000.
67. Bucaille, J.L., E. Felder , G. Hochstetter. Identification of the viscoplastic behavior of a polycarbonate based on experiments and numerical modeling of the nano-indentation test, *Journal of Materials Science*, 2002, 37: 3999-4011.
68. Zhang, C.Y., Y.W. Zhang, K.Y. Zeng, L. Shen. Nanoindentation of polymers with a sharp indenter. *J. Mater. Res.*, 2005, 20: 1597-1605 .
69. Kermouchea, G., J.L. Loubetb, J.M. Bergheau. Extraction of stress-strain curves of elastic-viscoplastic solids using conical/pyramidal indentation testing with application to polymers *Mechanics of Materials*, 2008, 40(4-5): 271-283.
70. Lu, H., B. Wang , J. Ma, G. Huang, H. Visthanatan. Measurement of Creep Compliance of Solid Polymers by Nanoindentation *Mechanics of Time-Dependent Materials*, 2003, 7(3): 189-207.
71. Ngan, A.H., B. Tang. Viscoelastic effects during unloading in depth-sensing indentation. *J. Mater. Res.*, 2002, 17: 2604-2610.
72. Fujisawa, N., M.V.Swain. Nanoindentation-derived elastic modulus of an amorphous polymer and its sensitivity to load-hold period and unloading strain rate. *J. Mater. Res.*, 2008, 23: 637-641.
73. Oyen, M. Sensitivity of polymer nanoindentation creep measurements to experimental variables. *Acta Materialia*, 2007, 55(11): 3633-3639.
74. Wei, Y., X. Wang, M. Zhao. Size effect measurement and characterization in nanoindentation test. *J. Mater. Res.*, 2004, 19: 208-217.

75. Hana, C., S. Nikolov. Indentation size effects in polymers and related rotation gradients. *J. Mater. Res.*, 2007, 22: 1662-1672.
76. Nikolov, S., C.S. Han, D. Raabe. *On the origin of size effects in small-strain elasticity of solid polymers*. *International Journal of Solids and Structures*, 2007, **44**: 1582–1592.
77. Fischer-Cripps, A.C. *Nanoindentation 2002*, New York: Springer-Verlag.
78. Smith, J.F., S. Zheng. High temperature nanoscale mechanical property measurements. *Surface Engineering*, 2000, 16: 143-146.
79. Beake, B.D. and J.F. Smith. High-temperature nanoindentation testing of fused silica and other materials, *Philosophical Magazine A*, 2002, 82: 2179-2186.
80. Beake, B.D., G.A. Bell, W. Brostow, W. Chonkaew. Nanoindentation creep and glass transition temperatures in polymers. *Polymer International*, 2007, 56: 63.
81. Hinz, M., A. Kleiner, S. Hild, O. Marti, U. Durig, B. Gotsmann, U. Drechsler, T.R. Albrecht, P. Vettiger. Temperature dependent nano indentation of thin polymer films with the scanning force microscope. *European Polymer Journal*, 2004, 40: 957–964.
82. Beake, B.D. Modelling indentation creep of polymers: a phenomenological approach. *J. Phys. D: Appl. Phys.*, 2006, 39: 4478–4485.
83. Sills, S., H. Fong, C. Buenviaje, M. Sarikaya, M. Overneya. Thermal transition measurements of polymer thin films by modulated nanoindentation. *Journal of applied physics*, 2005, 98: 014302.
84. Gray, A., D. Orecchia, B.D. Beake. Nanoindentation of Advanced Polymers Under Non-Ambient Conditions: Creep Modelling and Tan Delta. *Journal of Nanoscience and Nanotechnology*, 2008, 8:1-6.
85. Huber, N., E. Tyulyukovskiy. A new loading history for identification of viscoplastic properties by spherical indentation. *J. Mater. Res.*, 2004, 19: 101-113.
86. Odegard, G.M., T.S. Gates and H.M. Herring. Characterization of viscoelastic properties of polymeric materials through nanoindentation *Experimental Mechanics*, 2005, 45: 130-136.
87. Huang, G., B. Wang, H. Lu. Measurements of Viscoelastic Functions of Polymers in the Frequency-Domain Using Nanoindentation *Mechanics of Time-Dependent Materials*, 2004, 8: 345-364.

88. Singh, S.P., J.F. Smith, R.P. Singh. Characterization of the Damping Behavior of a Nanoindentation Instrument for Carrying Out Dynamic Experiments. *Experimental Mechanics*, 2007, 48: 571-583.
89. Loubet, J. L., W. C. Oliver, B. N. Lucas. Measurement of the loss tangent of low-density polyethylene with a nanoindentation technique. *J. Mater. Res.*, 2000, 15: 1195-1198.
90. White, C.C., M.R. VanLandingham , P.L. Drzal , N.K. Chang , S.H. Chang. Viscoelastic Characterization of Polymers Using Dynamic Instrumented Indentation. *Journal of Polymer Science Part B: Polymer Physics* 2005. 43(14): 1812-1824.
91. Herbert., E.G., W.C. Oliver , G.M. Pharr. Nanoindentation and the dynamic characterization of viscoelastic solids. *J. Phys. D: Appl. Phys.*, 2008, 41.
92. Singh, S.P., R.P. Singh, J.F. Smith. Displacement Modulation Based Dynamic Nanoindentation for Viscoelastic Material Characterization. in *Mater. Res. Soc.* 2005.
93. Li, X., B. Bhushan. A review of nanoindentation continuous stiffness measurement technique and its applications. *Materials Characterization*, 2002, 48: 11-36.
94. Tang, B., A.H.W. Negan. Accurate measurement of tip-sample contact size during nanoindentation of viscoelastic materials. *J. Mater. Res.*, 2003, 18: 1141-1148.
95. Xiea, X., Y. Maia, and X. Zhou. Dispersion and alignment of carbon nanotubes in polymer matrix: A review, *Materials Science and Engineering: R: Reports*, 2005. 49(4): 89-112.
96. Garmestani, H., et al., *Epoxy Mediated Alignment of Single Wall Carbon Nanotubes Under High Magnetic Fields*. *Advanced Materials*, 2003. **15**: p. 1918-1922.
96. Benicewicz, B. C., M.E. Smith, J D. Earls, R.D. Priester Jr, S.M. Setz, R.S. Duran, E. P. Douglas. Magnetic Field Orientation of Liquid Crystalline Epoxy Thermosets. *Macromolecules*, 1998, 31: 4730-4738.